ChemComm

REVIEW ARTICLE

Published on 18 May 2026
Licence and permissions

Check for updates

Cite this: *Chem. Commun.*, 2026, **62**, 11572

The application of oxyanion modulation in electrocatalysts for oxygen evolution reaction: a review

Yi-Xuan Zheng, Wei Liao, Yonghai Cao, Hongjuan Wang, Hao Yu and Hao-Fan Wang *

Developing oxygen evolution reaction (OER) electrocatalysts that possess both high activity and stability is of great significance for promoting the industrialization of hydrogen production technology through water electrolysis. The core bottleneck of this technology lies in the complex four-electron transfer process and harsh oxidative environment of the OER, resulting in sluggish reaction kinetics and severe catalyst corrosion. In recent years, various modulation strategies have been proposed to enhance the OER performance of catalysts, among which oxyanion ions have demonstrated unique dynamic and interfacial regulatory effects. This review summarizes the research progress over the past decade in the modulation of OER catalysts by oxyanion ions, focusing on their roles in dynamic sacrifice and reconstruction, promotion of reaction kinetics, modulation of the microenvironment, and activation of the lattice oxygen mechanism (LOM). Finally, current challenges faced in this research area are highlighted, and perspectives are provided for the future development of high-performance OER electrocatalysts.

Received 26th March 2026,
Accepted 15th May 2026

DOI: 10.1039/d6cc01844k

rsc.li/chemcomm

1 Introduction

Global warming and the depletion of fossil energy resources represent critical challenges to the realization of sustainable development.[1] In recent years, the growing severity of energy shortages and environmental degradation has necessitated the development of clean alternative energy sources. Hydrogen (H_2), characterized by its high energy density (120 MJ kg^{-1}), superior combustion efficiency, abundant availability, and zero-pollution emission, is widely regarded as an ideal substitute for fossil fuels.[2,3] Consequently, the large-scale and cost-effective production of high-purity hydrogen has remained a central research focus in the field of energy chemistry. Current industrial methods for hydrogen production include coal gasification, alcohol decomposition, methane reforming, and water splitting.[4] Among these, electrochemical water splitting is considered one of the most promising approaches for

School of Chemistry and Chemical Engineering, South China University of Technology, Guangzhou, 510641, China. E-mail: whf@scut.edu.cn



Yi-Xuan Zheng

Yi-Xuan Zheng is an undergraduate student majoring in Applied Chemistry at South China University of Technology. She is currently working under the guidance of Associate Professor Hao-Fan Wang. Her research focuses on the design and synthesis of efficient electrocatalysts for application in advanced energy materials.



Wei Liao

Wei Liao received his BS degree and MS degree from Guizhou University in 2019 and 2023, respectively. Currently he is a PhD candidate at South China University of Technology. His research focuses on the design and development of advanced transition-metal compounds for oxygen reduction/evolution and hydrogen evolution reactions.

This journal is © The Royal Society of Chemistry 2026

generating high-purity hydrogen, owing to the abundance of water resources, the absence of greenhouse gas emissions, high dissociation efficiency, and high product purity.[5,6] In contrast to the hydrogen evolution reaction (HER) occurring at the cathode, the anodic oxygen evolution reaction (OER) in this technology involves a four-electron transfer process, which exhibits sluggish reaction kinetics and high overpotential, significantly impeding large-scale hydrogen production *via* water electrolysis.[7–10] Moreover, the high potential region where the OER occurs creates a strongly oxidizing environment that accelerates catalyst corrosion. Therefore, the design and development of OER electrocatalysts that simultaneously exhibit high activity and long-term stability, thereby effectively lowering reaction energy barriers and accelerating reaction kinetics, is crucial for overcoming current technological bottlenecks and advancing the industrial application of water electrolysis technologies.[11]

In response to the aforementioned performance bottlenecks of the OER, researchers have dedicated efforts to the precise optimization of electrocatalyst design strategies from multiple dimensions. Following the research boom centred on cation modulation, the influence of anion modulation on electrocatalysts has gradually attracted increasingly widespread attention.[12,13] In metal compounds, anions constitute the primary coordination environment of metal sites, thereby shaping their electronic structure. Anions can act as electron donors, regulating the state of cations through electronic interactions, and the properties of the anions determine their interaction characteristics with cations as well as the reactivity of the active sites.[14–16] Simple anions, such as S^{2-}, Se^{2-}, and P^{3-}, have been demonstrated to enhance OER catalytic performance through various pathways, including inducing pre-catalyst reconstruction, modulating the oxidation state of metal centres, optimizing the electronic structure, and promoting reaction kinetics.[14,17–21]



Yonghai Cao

Dr Yonghai Cao received his B.E. degree from Xiangtan University in 2009 and PhD degree from South China University of Technology in 2014. He joined the School of Chemistry and Chemical Engineering at South China University of Technology in 2017. His main research interests are focused on the synthesis and application of nanomaterials in the field of catalysis and environmental remediation.



Hongjuan Wang

Hongjuan Wang obtained her BSc in Fine Chemical Engineering from Zhengzhou University of Light Industry in 1997 and her PhD degree in Chemical Engineering from South China University of Technology under the supervision of Prof. Zhong Li in 2003. She then joined Prof. Feng Peng's group at South China University of Technology as an assistant research fellow. In 2010, she was promoted to an associate professor of South China University of Technology. Her research interests include nanocatalytic materials and their application in the energy electrocatalysis field.



Hao Yu

Professor Hao Yu received his Bachelor's degree in 1999 and PhD in 2005 from Tsinghua University. He has been teaching at South China University of Technology since 2005. He has published 200+ papers in peer-reviewed journals and has been granted 20 Chinese invention patents and 1 U.S. patent as the first inventor. His research interests include the development of carbon-based catalysts and their energy/environment related applications, electrified chemical processes and reaction engineering.



Hao-Fan Wang

Hao-Fan Wang received his BE and PhD degrees from the Department of Chemical Engineering, Tsinghua University, in 2013 and 2018, respectively. Then he worked as a postdoctoral researcher at the National Institute of Advanced Industrial Science and Technology (AIST), Japan. In 2022, he joined the School of Chemistry and Chemical Engineering, South China University of Technology, as an associate professor. His research focuses on the design, synthesis and regulation of precious-metal-free electrocatalysts for oxygen- and hydrogen-related energy conversion and storage systems.

Li *et al.* selected thioacetamide (TAA) as a sulfur source to sulfurize nickel-iron layered double hydroxide (NiFe LDH), preparing NiFeS-*x* electrocatalysts. By regulating the atomic ratio of S and O, the team successfully modulated the electronic structure of the active sites and the covalency/ionicity of the interaction between cations and anions, thereby optimizing OER performance.[15] Gu *et al.* reported an anion modulation strategy involving the doping of iodide ions into the CuS lattice. Their study indicated that the introduction of iodide ions effectively regulates the dynamic surface reconstruction behaviour of the catalyst and induces the generation of active reaction sites, thereby significantly enhancing OER catalytic activity while ensuring excellent catalyst stability.[22] Zheng *et al.* proposed a fluoride ion modulation strategy to achieve efficient and stable OER performance of RuO_2 under acidic conditions.[23] The research pointed out that the moderate hydrogen bonding interactions induced by fluoride ions can effectively accelerate the deprotonation process of oxygen-containing intermediates and water molecules, enhancing the reaction kinetics. Concurrently, the high electronegativity of fluoride ions helps weaken the covalency of the Ru–O bond, strengthening the catalyst's stability.

To further improve the structural stability of catalysts under high potentials and their intrinsic catalytic activity, increasing studies have begun to focus on the performance modulation role of oxyanions such as SO_4^{2-}, NO_3^-, PO_4^{3-} and MoO_4^{2-} in the OER.[24–27] Compared to simple anions, oxyanions, due to the introduction of oxygen atoms within their framework, typically exhibit higher electronegativity. This facilitates a more profound modulation of the d-band centre position of the active metal, thereby optimizing the adsorption energy of oxygen-containing reaction intermediates and potentially overcoming the inherent theoretical overpotential limitation of the OER.[28–31] Furthermore, oxyanions possess basic oxygen sites, larger ionic radii, and unique polyhedral structures, which are distinct from simple anions. This enables them to achieve synergistic optimization of the OER process from multiple dimensions, including electronic regulation, proton transfer, and spatial configuration, demonstrating a more comprehensive modulation capability. Notably, even in systems where simple anions serve as the primary regulatory units, species such as S^{2-} and Se^{2-} are susceptible to *in situ* oxidation under the high potentials characteristic of the OER, ultimately transforming into their corresponding oxyanions.[32,33] Furthermore, recent studies have convincingly demonstrated that these *in situ* generated oxyanions, rather than the original simple anions, are the genuine source of the enhanced OER activity.[34,35] This phenomenon implies that the regulatory influence of oxyanions is not restricted to systems where they are directly introduced, but is also prevalent in catalysts derived from simple anion precursors, thereby demonstrating broad relevance. Consequently, a fundamental understanding of oxyanion mediated regulation mechanisms is of paramount importance for the rational design of high performance OER electrocatalysts.

Numerous studies have highlighted the crucial regulatory effects of oxyanions on the OER process. Although some existing reviews have discussed this topic from specific perspectives, such as chemisorption, surface reconstruction, or organic molecule oxidation, a comprehensive review dedicated to systematically elucidating the multidimensional modulation mechanisms of oxyanions remains lacking.[36–39] It is worth noting that, while introducing oxyanions into the electrolyte as additives has also been proven effective in promoting OER kinetics, to provide a more focused and in-depth overview, the scope of "oxyanion modulation" discussed herein is strictly confined to the modification of the catalyst materials themselves, without involving alterations to the electrolyte.[40–43] Based on the defined scope, this review aims to systematically summarize the key functions of oxyanions in OER catalysts, including the dynamic sacrificial and reconstruction behaviours of oxyanions, their accelerating effect on proton-coupled electron transfer (PCET) processes, the modulation of the local catalyst micro-environment, the optimization of adsorption energies of reaction intermediates, the alteration of the rate-determining step (RDS), and the activation and regulation of the lattice oxygen mechanism (LOM). Finally, the current challenges facing oxyanion modulation strategies are discussed, and future development directions are proposed. We anticipate that this review will provide valuable insights for a deeper understanding of the regulatory mechanisms and structure–activity relationships of oxyanions, thereby offering inspiration for the design and development of high-performance water splitting catalysts and energy materials.

2 Oxyanions for catalyst reconstruction through self-sacrificing

During the OER process catalysed by oxyanion-containing materials, oxyanions face competitive adsorption from both reaction intermediates and electrolyte ions, leading to their dynamic adsorption and dissolution.[36] For instance, under alkaline conditions, CO_3^{2-} generated from the dissolution of atmospheric CO_2 into the electrolyte can gradually exchange various intercalated anions originally present in NiFe LDH.[44–48] Traditionally, such ion exchange processes were considered unfavourable, as they accelerate structural collapse and compromise catalyst stability. However, recent studies have revealed that the controlled sacrificial behaviour of oxyanions can effectively mediate the *in situ* reconstruction and morphological evolution of the catalyst, holding positive significance for optimizing its microstructure and enhancing catalytic performance. This section summarizes the key findings in this emerging area.

2.1 Inducing intrinsic active phase formation

Studies have demonstrated that transition metal (oxy)hydroxide (MOOH) species formed through *in situ* surface reconstruction exhibit higher catalytic activity than pristine sites derived from static design and are widely recognized as the true active species for the alkaline OER.[49–52] Furthermore, Zhong *et al.* proposed that although the reconstructed MOOH shares similar

 This journal is © The Royal Society of Chemistry 2026

microstructural features with directly synthesized MOOH, it typically displays superior catalytic activity.[53] An increasing body of research confirms that the leaching behaviour of oxyanions can induce the oxidation of active metals and drive the *in situ* reconstruction of catalytic materials into highly active catalytic phases. Oxyanions, particularly those with appreciable solubility in alkaline electrolytes, are frequently employed to mediate this reconstruction process.[54–58] Notably, the effective reconstruction of MOOH active phases containing high-valence metal species and the generation of the true active phase are contingent upon the oxidation of active metals within the precursor.[59–61] Research reported by Liu *et al.* indicates that during electrocatalytic reactions, precursors containing simple anions (*e.g.*, sulfides and basic salts) undergo oxidation of lattice anions such as S^{2-} and Se^{2-} into oxyanions, which subsequently leach into the electrolyte.[38] This process not only triggers deep structural reconstruction of the catalyst but also promotes the oxidation of metal centres to higher valence states (*e.g.*, Co^{4+} and $Ni^{3+\delta}$), ultimately forming the true active phase centred on MOOH, thereby significantly enhancing catalytic performance. Liao and co-workers reported a strategy modulating nickel-iron (oxy)-hydroxide (NiFeOOH) with SO_4^{2-} to enhance OER performance.[62] Their study demonstrated that SO_4^{2-} leaches from the catalyst into the electrolyte during the initial reaction stages. This loss of SO_4^{2-} accelerates the electrochemical reconstruction of the pre-catalyst, enabling its more rapid conversion at lower potentials into the true catalytically active phase, namely high-valence NiFeOOH. Furthermore, in the NiMoFeO@NC material system, the leaching of MoO_4^{2-} facilitates the reconstruction of the material into the active species Ni(Fe)OOH, thereby enhancing its OER catalytic performance.[64] Similarly, the leaching of PO_4^{3-} can induce the surface reconstruction of $Ni_{1.5}Sn@triMPO_4$ into Ni(Fe)OOH, effectively boosting the material's OER activity.[65] Beyond the aforementioned oxyanions, the leaching of SeO_3^{2-} can also induce *in situ* catalyst reconstruction, and the electrochemical leaching of SeO_3^{2-} accelerates the transformation of $NiSe_2$ to NiOOH, achieving high OER activity for the material.[66] Liang *et al.* proposed an "anion leaching-metal oxidation" model, clarifying that within the $Co(OH)(CO_3)_{0.5}$/NF material, the leaching of CO_3^{2-} plays a central role in inducing material reconstruction and the formation of highly active Co(IV).[63] As shown in Fig. 1a, the X-ray diffraction (XRD) patterns of $Co(OH)_x(A)_y$-AR remain largely unchanged after OER, indicating that the bulk phase of the basic cobalt salts is generally preserved. In contrast, CoOOH diffraction peaks appear in $Co(OH)_2$-AR, suggesting that the nature of the interlayer anion strongly influences the reconstruction pathway during OER. The post reaction Co 2p X-ray photoelectron spectroscopy (XPS) spectra in Fig. 1b further reveal the disappearance of the Co(II) satellite peaks together with the emergence of Co(III) and Co(IV) features, confirming the progressive surface oxidation from Co(II) to Co(III) and then to Co(IV), which is closely associated with the generation of the real active phase. Meanwhile, Fig. 1c shows that no detectable CO_3^{2-} signal remains in the surface shell of $Co(OH)(CO_3)_{0.5}$-AR, indicating substantial leaching of lattice CO_3^{2-} from the surface region. Combined with the structural information in Fig. 1d, these results suggest that CO_3^{2-} leaching creates surface defect sites and facilitates the oxidation of surface

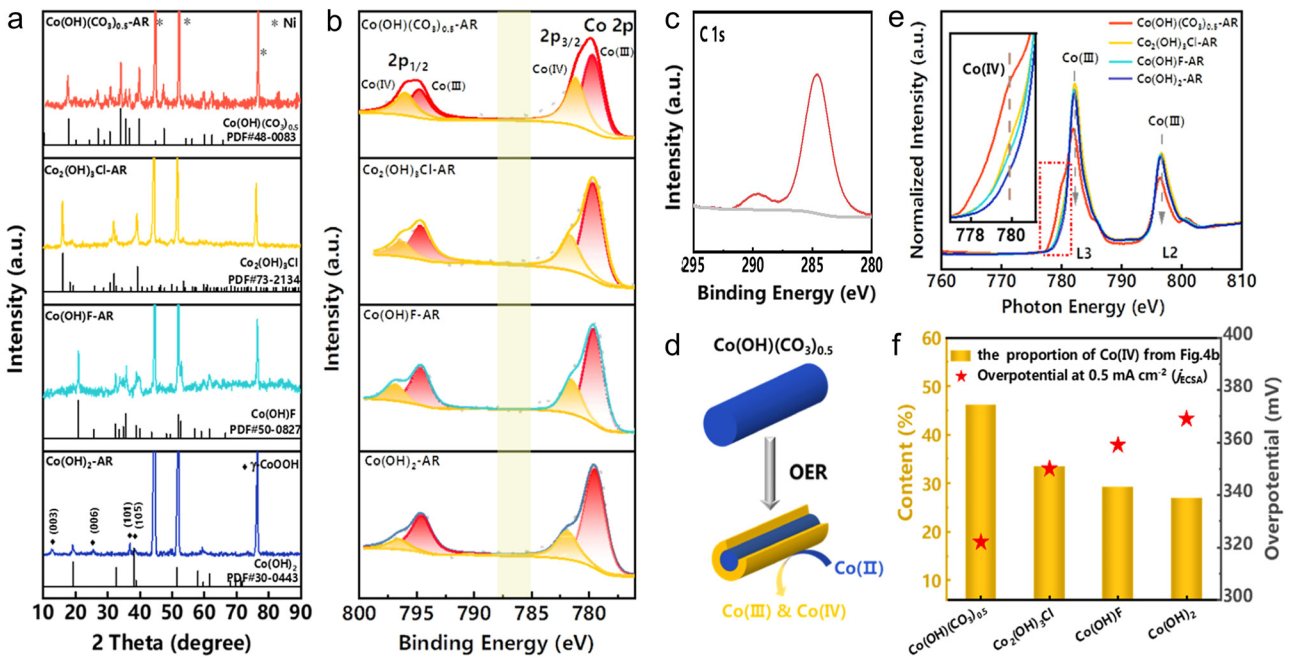

Fig. 1 Spectroscopic characterization of the catalysts-AR. (a) XRD pattern and (b) Co 2p XPS spectra of $Co(OH)(CO_3)_{0.5}$/NF-AR, $Co_2(OH)_3Cl$/NF-AR, Co(OH)F/NF-AR, and $Co(OH)_2$/NF-AR. (c) C 1s spectra of $Co(OH)(CO_3)_{0.5}$/NF-AR. (d) Schematic diagram of the structure evolution of the $Co(OH)(CO_3)_{0.5}$/NF sample during the OER process. (e) Normalized Co L-edge SXAS of the samples. (f) Summary of the overpotential and Co(IV) content in the catalysts-AR.[63] Reproduced with permission. Copyright 2023, American Chemical Society.

Co species into highly active Co(IV) centres during OER. As summarized in Fig. 1f, this work demonstrates that specific anion leaching can effectively regulate catalyst reconstruction and increase the abundance of active Co(IV) species, thereby enhancing OER performance. Ma *et al.*, utilizing $Co_2(OH)_3Cl$@$NiMoO_4$ as a precatalyst, demonstrated that the synergistic dual-ion leaching of the oxyanion MoO_4^{2-} and the simple anion Cl^- can induce continuous self-reconstruction of the material. This process promotes the oxidation of Co and Ni metal centres, ultimately forming a CoOOH@NiOOH heterojunction as the true active centre for OER.[67] As shown in Fig. 2, *in situ* FTIR and Raman spectra analyses confirmed the release of Mo species from the precursor together with the concurrent formation of CoOOH and NiOOH phases, highlighting the key role of specific anion leaching in regulating catalyst reconstruction and enhancing OER activity.

As discussed above, the leaching of oxyanions alters the original coordination environment of the metal active sites. This direct electronic effect, induced by the change in the coordination environment, drives the metal centres to transition to higher oxidation states, thereby generating the true active phase MOOH. Furthermore, studies have demonstrated that the dissolution of oxyanions simultaneously leads to a transformation in the catalyst's morphology. This process increases the material's porosity, allowing numerous metal sites originally embedded in the bulk phase to be exposed to the alkaline electrolyte. Consequently, this enhances the permeation and mass transfer between the active centres and reactants, ensuring the deep oxidation of the metal active sites.[53,68–70] Therefore, the direct electronic effect and the secondary effect of increased contact sites play a highly synergistic and positive role in the oxidation of the active sites and the reconstruction of the catalyst.

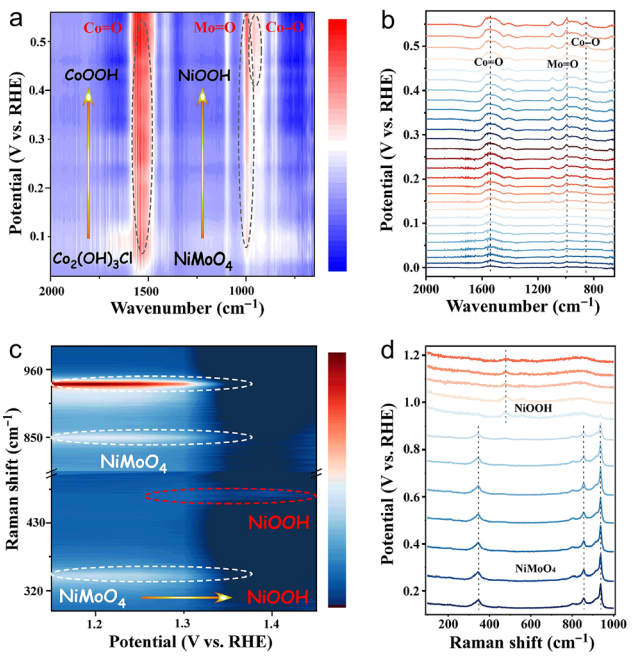

Fig. 2 *In situ* FT-IR and Raman characterization of $Co_2(OH)_3Cl$@$NiMoO_4$. (a) Two-dimensional (2D) contour diagram and (b) referred line plot of *in situ* FT-IR spectroscopy of $Co_2(OH)_3Cl$@$NiMoO_4$ in 1.0 M KOH during OER. (c) 2D contour diagram and (d) referred line plot of *in situ* Raman spectroscopy without applied bias of $Co_2(OH)_3Cl$@$NiMoO_4$ in 1.0 M KOH during OER.[67] Reproduced with permission. Copyright 2024, Springer Nature.

It is worth emphasizing that the MOOH generated through precursor reconstruction, serving as the genuine active phase for the catalytic reaction, indeed exhibits superior intrinsic activity. However, it must be explicitly distinguished that the oxyanions retained within the host lattice/interlayer or adsorbed on the catalyst surface during reconstruction are by no means mere structural byproducts; they also possess independent and direct mechanisms for electronic structure modulation and reaction kinetics promotion. To this end, the rational construction of pure MOOH models and oxyanion-MOOH models for in-depth theoretical calculations is particularly essential to further decouple and elucidate the authentic contribution of oxyanions.[71–73] Overall, the presence of oxyanions not only facilitates the initial formation of the true MOOH active centres but also generates a synergistic effect with MOOH at the microscopic level, thereby collectively driving a further leap in catalytic performance.

2.2 Directing morphological evolution

The controlled sacrifice of oxyanions not only effectively induces *in situ* reconstruction of catalytic materials but can also serve as a morphology-directing agent, mediating the morphological evolution of the catalyst and thereby increasing the electrochemically active surface area of the material. A growing body of research indicates that the leaching or exchange behaviour of oxyanions can endow the resulting catalyst with a larger electrochemically active surface area, higher porosity, and more abundant catalytic active sites.[74–77] T. Kahlstorf and co-workers extended the sacrificial leaching mechanism of oxyanions to water-soluble nickel/iron nitrate systems, demonstrating that under alkaline OER conditions, NO_3^- can act as a beneficial sacrificial agent, leaching out and driving the rapid reconstruction of water-soluble nitrates into porous Ni(Fe)OOH, the true active centre for the OER.[78] Ni(Fe)OOH, characterized by its unique porous structure rich in defect sites, exhibited exceptional electrocatalytic performance. Cui *et al.*, investigating molybdate-based h-$NiFeMoO_x$, further confirmed that the leaching of MoO_4^{2-} during electrochemical reconstruction is a key mechanism for optimizing catalyst structure and performance.[79] Scanning electron microscopy (SEM) and transmission electron microscopy (TEM) images in Fig. 3a and b reveal a pronounced structural evolution from the initial micron sized solid pillar morphology to a loosely stacked nanosheet architecture. Combined with the XRD result in Fig. 3c and the high resolution transmission electron microscope (HRTEM) analyses in Fig. 3d, the reconstructed phase can be identified as short range ordered but long range disordered β-$Ni_{0.84}Fe_{0.16}OOH$. This profound structural and phase transformation is fundamentally driven by the dissolution and leaching of MoO_4^{2-} from the precursor, which is

This journal is © The Royal Society of Chemistry 2026

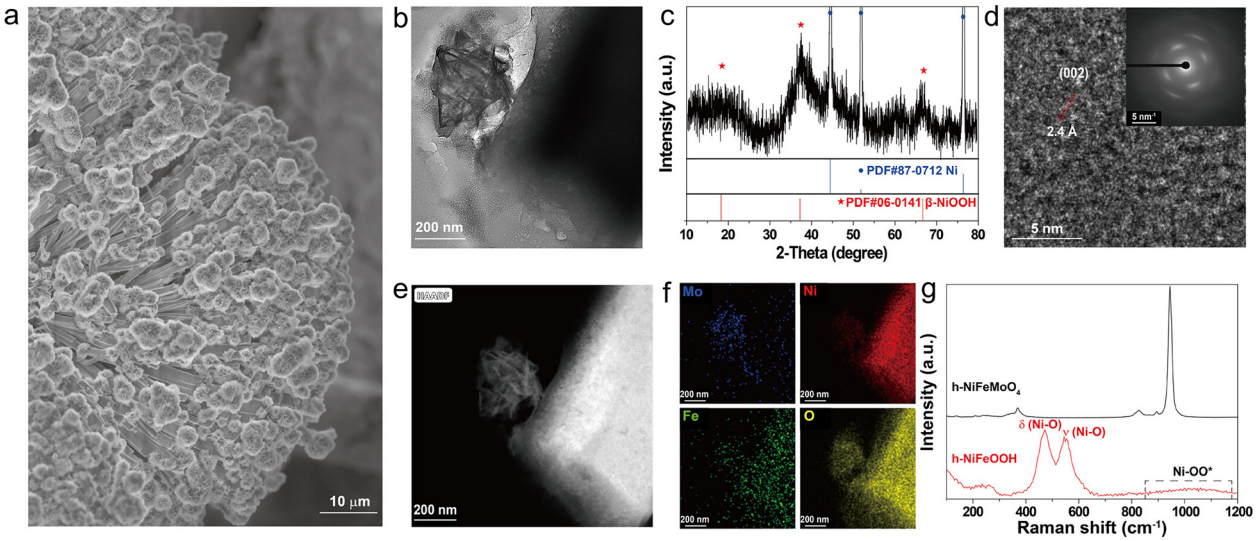

Fig. 3 Characterization after the reconstruction of the precatalyst. (a) Low-magnification SEM image, (b) TEM, (c) XRD pattern, (d and inset) HRTEM image with the SAED pattern, (e) HAADF-STEM image, and (f) STEM-EDX elemental mapping of Mo, Ni, Fe, and O in h-NiFeOOH. (g) Raman spectra of h-NiFeMoO$_x$ and h-NiFeOOH.[79] Reproduced with permission. Copyright 2025, American Chemical Society.

explicitly confirmed by the removal of Mo species in the energy dispersive X-ray spectroscopy (EDS) mapping in Fig. 3f and the Raman spectra in Fig. 3g. Ultimately, such reconstruction preserves the overall structural framework while introducing abundant defect sites through anion leaching, thereby increasing surface area and porosity and facilitating both exposure of active sites and mass transport during the OER.

2.3 Leveraging leaching and re-adsorption dynamics

In the dynamic heterogeneous catalysis process of the OER, the electrode–electrolyte interface is not in a static state but is continuously accompanied by dynamic species exchange and structural evolution of the catalyst. A study in 2020 indicated that during electrolysis, soluble oxyanions generated from the oxidation of precatalysts can be re-adsorbed onto the active catalyst surface through electrostatic interactions under the influence of the electric field.[80] This mechanism breaks through the traditional perspective that anion leaching inevitably leads to catalytic performance degradation, revealing a dynamic equilibrium cycle characterized by both self-activation and self-regulation. The core logic of this dynamic cycle lies in the synergistic effect between ''sacrifice'' and ''compensation''. On the one hand, as discussed previously, the functional leaching of oxyanions is a key driving force triggering the deep reconstruction of precatalysts into highly active (oxy)hydroxides (*e.g.*, NiFeOOH). Through selective dissolution, these anions accelerate the evolution of the active phase while inducing the formation of abundant oxygen vacancies, providing more effective active sites for the OER. On the other hand, oxyanions dissolved in the electrical double layer exhibit dynamic re-adsorption behaviour under the electric field. By optimizing the electronic cloud distribution and d-band centre position of the active sites, they specifically stabilize key intermediates such as *OOH, thereby significantly reducing the energy barrier of the rate-determining step of the catalytic reaction. Research by Liao and his team revealed the enhancing effect of the leaching–re-adsorption dynamic behaviour of MoO_4^{2-} on OER activity.[81] The study showed that during the leaching process, MoO_4^{2-} promotes the rapid reconstruction of the precatalyst into the NiFeOOH active phase, while its re-adsorption behaviour optimizes the electronic structure of the active sites, enhancing their ability to capture *OOH intermediates and accelerating the reaction progress. The synergistic action of these two aspects achieves enhanced catalytic performance. Beyond MoO_4^{2-}, VO_4^{3-} has also been confirmed to trigger a similar leaching–re-adsorption synergistic effect.[82] Ma *et al.* proposed that during the controlled dissolution of VO_4^{3-}, while inducing the reconstruction of the catalyst surface into NiFeOOH, it promotes the formation of ample oxygen vacancies. The re-adsorption of VO_4^{3-} synergistically optimizes the adsorption energy of OH^-, significantly lowering the energy barrier of the rate-determining step (*OH → *O) in the OER, thereby enhancing the catalytic reaction kinetics. Liu *et al.* further confirmed through experiments that interlayer NO_3^- in iron-nickel nitrate hydroxide (FeNiNH) desorbs and dissolves into the electrolyte during the alkaline OER process. Subsequently, the dissolved NO_3^- can re-adsorb onto the catalyst surface, reducing OER overpotential by stabilizing the reaction intermediate *OOH.[83] As shown in Fig. 4a–d, XPS and *in situ* Raman spectra results consistently confirm the gradual disappearance of lattice NO_3^- during the reconstruction process. More importantly, electrochemical measurements in different electrolytes, including pristine KOH, freshly prepared NO_3^--free KOH, and KOH containing additional KNO_3, provide further evidence that re-adsorbed NO_3^- plays a beneficial role in OER catalysis (Fig. 4e and f). In particular, the catalyst shows inferior activity in the NO_3^--free electrolyte but improved performance when extra NO_3^- is introduced, indicating that

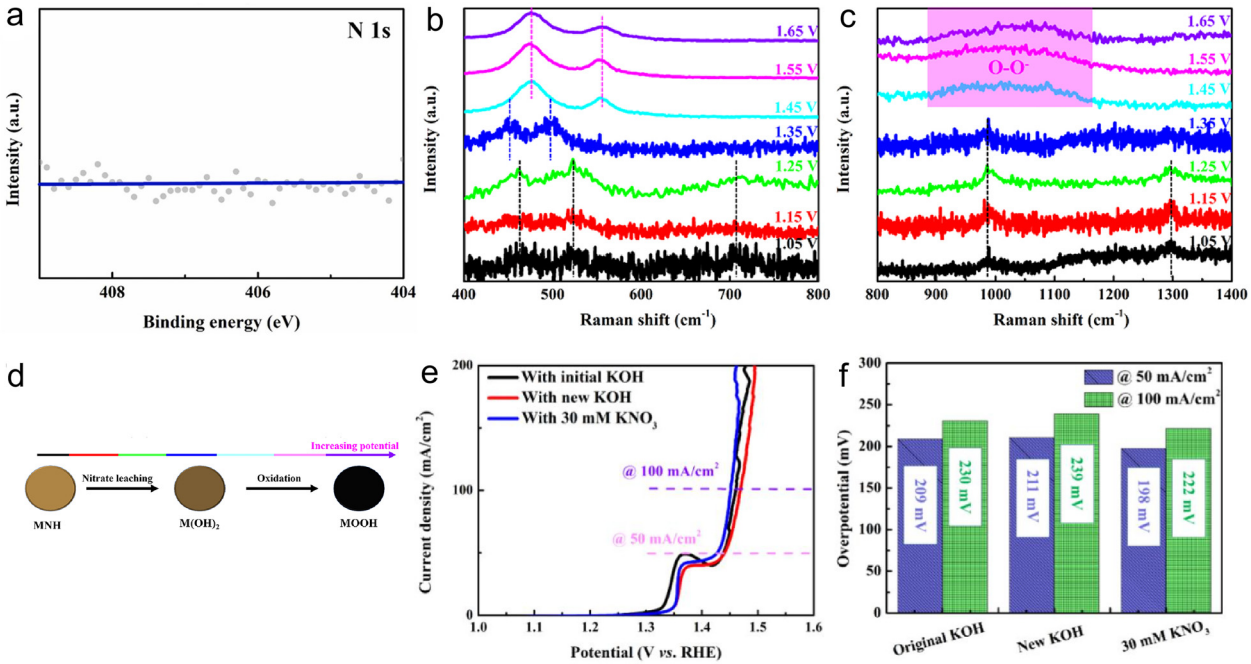

Fig. 4 (a) High-resolution XPS patterns of N 1s. (b) Potential-dependent Raman spectra of Fe_1Ni_9NH in the range 400–800 cm^{-1}, (c) potential-dependent Raman spectra of Fe_1Ni_9NH in the range 800–1400 cm^{-1}, and (d) structural transformation with increasing potential. (e) LSV curves of Fe_1Ni_9NH measured with initial KOH, new KOH, and KOH + 30 mM KNO_3 electrolyte, and (f) corresponding overpotentials at 50 and 100 mA cm^{-2}.[83] Reproduced with permission. Copyright 2022, Elsevier.

surface adsorbed NO_3^- can stabilize the key *OOH intermediate and thereby reduce the OER overpotential. These results highlight that the dissolution and subsequent re-adsorption of NO_3^- constitute an important dynamic regulation pathway for enhancing OER performance in this system. These conclusions are also applicable in seawater electrolysis systems. Zhou *et al.* showed that MoO_4^{2-} leaching can effectively promote catalyst reconstruction and accelerate the conversion of NiFe based precatalysts into the highly active NiFeOOH phase during seawater electrolysis.[84] More importantly, the dissolved MoO_4^{2-} can reabsorb on the reconstructed surface and serve as an electronic structure regulator, thereby optimizing the local charge distribution of the active sites and improving catalyst stability against chloride corrosion. As shown in Fig. 5a–d, *in situ* Raman spectra, XPS, and electrochemical analyses consistently indicate that Mo species are gradually oxidized and released as soluble MoO_4^{2-} during anodic polarization, which markedly facilitates the formation of the NiFeOOH active phase. Compared with the Mo-free Fe-NiP_x/NF, the FeMo-NiP_x/NF catalyst undergoes reconstruction at a lower potential and exhibits a higher degree of phase transformation. In addition, the reappearance of Mo related Raman signals after operation, together with the recovery of the Mo^{6+} XPS feature in Fig. 5c, further suggests the re-adsorption of MoO_4^{2-} on the active NiFeOOH surface, revealing a dynamic leaching and re-adsorption process. DFT calculations in Fig. 5e–h further show that MoO_4^{2-} preferentially adsorbs on Ni sites and induces electron redistribution over the Ni and Fe centres, which shifts the d band centre and strengthens the adsorption of key oxygenated intermediates, thus lowering the OER energy barrier. Meanwhile, the re-adsorbed MoO_4^{2-} also helps suppress chloride induced corrosion through electrostatic repulsion, enabling the catalyst to deliver both high activity and good stability in overall seawater splitting.

3 Oxyanions for proton transfer and pH modulation

In alkaline or neutral media, the dissociation of water molecules and the subsequent surface deprotonation step (*OH → $*O + H^+ + e^-$) often encounter a substantial kinetic barrier, even becoming the RDS of OER.[85,86] Currently, the complex reaction kinetics of OER preclude a fully unified understanding of its specific mechanism. According to the classical adsorbate evolution mechanism (AEM), the OER involves a four-electron-four-proton PCET process at the metal centre surface, accompanied by the formation and evolution of various oxygen-containing intermediates such as *OH, *O, and *OOH on the metal cation sites.[87] Due to the significantly larger mass of protons compared to electrons, an imbalance between electron transfer and proton transfer can easily occur, leading to sluggish OER kinetics.[88] However, regardless of the subtle mechanistic variations in the OER, accelerating the slow proton transport dynamics remains key to enhancing the efficiency of the water oxidation reaction. An efficient PCET process can effectively avoid charge accumulation at the active sites, thereby lowering the activation energy barrier of the reaction.[89]

 This journal is © The Royal Society of Chemistry 2026

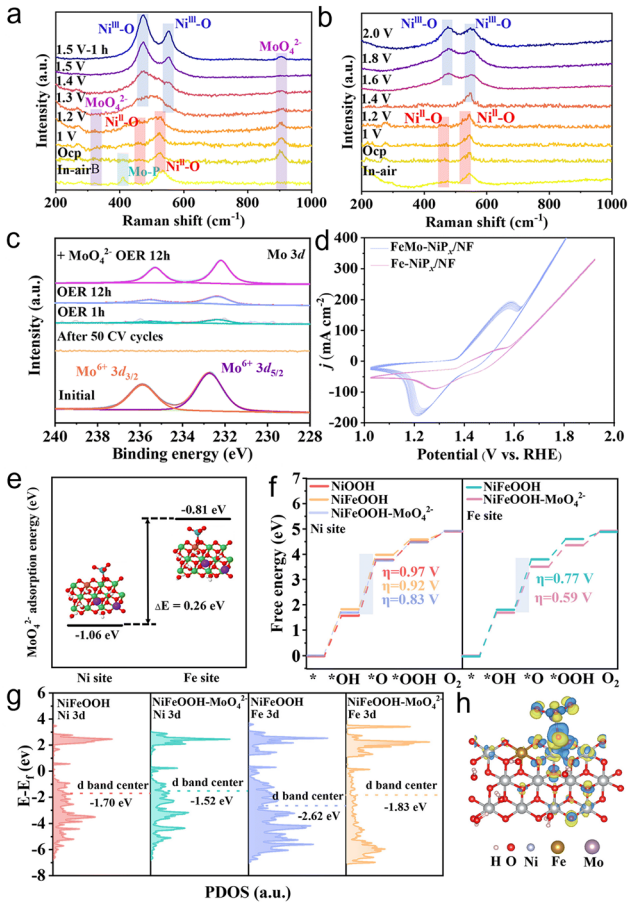

Fig. 5 Potential-dependent *in situ* Raman spectra of (a) FeMo-NiP_x/NF and (b) Fe-NiP_x/NF in 1.0 M KOH. (c) High-resolution Mo 3d XPS of FeMo-NiP_x/NF after different OER operation times (orange line, 50 CV cycles; green line, 1 h OER; blue line, 12 h OER in 1.0 M KOH; and magenta line, 12 h OER in MoO_4^{2-}-containing KOH). (d) CV curves of FeMo-NiP_x/NF and Fe-NiP_x/NF in the range of 1.0–1.9 V at a scan rate of 50 mV s^{-1}. (e) Adsorption energy of MoO_4^{2-} at the Ni and Fe sites of NiFeOOH. (f) Gibbs free energy profiles of the OER over NiOOH, Ni (left), and Fe (right) sites of NiFeOOH and NiFeOOH-MoO_4^{2-}. (g) The calculated PDOS of Ni 3d and Fe 3d in NiFeOOH and NiFeOOH-MoO_4^{2-}. (h) Differential charge densities of NiFeOOH when MoO_4^{2-} is adsorbed at the Ni site (yellow and blue areas denote electron accumulation and depletion, respectively).[84] Reproduced with permission. Copyright 2024, Royal Society of Chemistry.

3.1 Exploiting basicity for proton transfer

In traditional catalyst design, anion modulation (primarily referring to the introduction of simple anions such as S^{2-} and Se^{2-}) has mainly focused on optimizing the electronic structure of metal centres, *i.e.*, achieving modulation at the electronic level.[12,90,91] In contrast, oxyanions, as typical Brønsted bases or Lewis bases, possess unique proton affinity capabilities. This dual "electronic–proton modulation" mechanism is a key distinguishing feature of oxyanion modulation compared to simple anion strategies. Oxyanions such as PO_4^{3-}, $RCOO^-$, $C_2O_4^{2-}$ and SeO_3^{2-} can function as built-in bases or proton relays within the catalyst, facilitating the balance between electron and proton transfer by abstracting protons from intermediates.[92] He *et al.* proposed that oxyanions as built-in bases can assist proton transfer. For instance, tripropylamine (TPA) or electron-rich $RCOO^-$ and SO_3^{2-} can serve as proton acceptors, accelerating O–H bond cleavage by capturing protons from intermediates like *OH, thereby balancing the electron and proton transfer rates and, to some extent, overcoming the kinetic bottleneck of the OER.[39,93–96] Ding *et al.* suggested that PO_4^{3-} intercalated within NiFe LDH layers acts as an electron-rich Lewis base, capable of assisting proton transfer and thus balancing the PCET process.[97] Similarly, chemisorbed borate and its derivatives also exhibit the property of accelerating proton transfer.[37] The weak acidity of boric acid renders the borate anion $B(OH)_4^-$ a strong base, enabling it to accept protons generated from H_2O dissociation during the OER, thereby enhancing the proton transfer rate.[98–100] Concurrently, the efficient proton transfer capability of borate and its derivatives endows them with high activity and suitability in neutral water oxidation systems as well.[101,102]

3.2 Driving proton shuttling *via* multistage equilibria

Simple anions typically lack effective proton acceptor sites and do not possess the multi-step protonation/deprotonation capacity characteristic of oxyanions. Consequently, they struggle to directly assist interfacial proton capture and transport, lack acid–base buffering capacity, and cannot directly participate in the proton transfer process.[103,104] Oxyanions, exemplified by PO_4^{3-}, exhibit a multi-step protonation/deprotonation equilibrium involving $PO_4^{3-}/HPO_4^{2-}/H_2PO_4^-$.[105,106] They can not only modulate the electronic structure of the active centre but also act as a medium for proton transfer at the interface, directly participating in and accelerating proton transport and release. In 2025, Zhang *et al.* introduced the novel concept of phosphate ions functioning as a "proton bus".[107] Using NiCoP@NF as a model system, they showed that PO_4^{3-} participates in a reversible protonation and deprotonation process, thereby facilitating proton transfer between the catalyst surface and the electrolyte. As shown in Fig. 6a–c, *in situ* Raman spectra reveal the emergence and gradual intensification of the ν_s(P–OH) band at 813 cm^{-1} with increasing potential, indicating the protonation of phosphate species during electrooxidation. Meanwhile, the O–O stretching signal assigned to the O_2^{2-} intermediate appears at a lower potential in NiCoP@NF than in the phosphate-free NiCo@NF system, suggesting that phosphate-mediated proton transfer accelerates intermediate deprotonation and promotes the onset of the lattice oxygen mechanism. Further evidence is provided by the pH dependent activity analysis in Fig. 6d. NiCoP@NF shows a higher proton reaction order than the control sample, indicating a stronger kinetic dependence on proton transfer and supporting the presence of an efficient proton capture, transfer, and release cycle on the catalyst surface. These results suggest that phosphate species are not simply removed during reconstruction, but can remain dynamically involved in the catalytic process. Through their reversible protonation and deprotonation behaviour, they help reduce proton transport resistance and offer an effective route for improving OER kinetics.

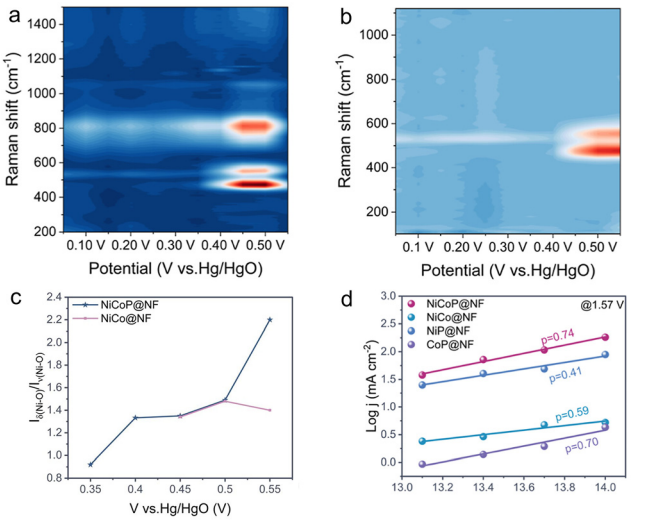

Fig. 6 *In situ* Raman spectra of (a) NiCoP@NF and (b) NiCo@NF. (c) The δ(Ni-O)-to-ν(Ni-O) ratios at different operational potentials in the *in situ* Raman spectra. (d) At 1.57 V (*versus* RHE), the current changes with the pH value of different samples.[107] Reproduced with permission. Copyright 2025, American Chemical Society.

3.3 Stabilizing interfacial microenvironment

Beyond the two aspects mentioned above, the acid–base properties and multi-step ionization characteristics of oxyanions also contribute significantly to local pH buffering and microenvironment modulation in the OER. In recent years, the "microenvironment effect" has garnered widespread attention among researchers.[108–110] In the OER, the properties of the microenvironment at the electrode/electrolyte interface often dictate the ultimate kinetic behaviour of the reaction.[111] Although most OER electrochemical performance tests are conducted under alkaline conditions (*e.g.*, common electrolyte systems like 1 M KOH), the vigorous reaction at high current densities can lead to significant differences between the local chemical environment at the electrode surface and the bulk solution. Specifically, the formation of a local acidic microenvironment on the surface of the anode catalyst during water electrolysis raises critical issues regarding catalyst stability.[112–114] The formation of this acidic microenvironment stems from the slow migration rate of OH^- from the membrane to the catalytic sites, which fails to promptly neutralize the H^+ generated during the deprotonation of electrolytic intermediates (*e.g.*, MO–H and MOO–H).[115–117] As discussed previously, by virtue of their unique amphoteric nature and multi-step ionization characteristics, oxyanions can construct a dynamic pH buffer layer on the catalyst surface, effectively mitigating sharp fluctuations in interfacial pH. This creates a kinetically more favourable and thermodynamically more stable reaction environment for the OER on a microscopic scale.[101,102] Relevant studies have fully confirmed the role of oxyanions in microenvironment modulation. Fan *et al.* introduced squarate anions (Sq^{2-}) into a NiOOH system. *In situ* spectroscopic characterization revealed that Sq^{2-} could capture OH^- through hydrogen bonding, delaying the formation of a local acidic microenvironment and thereby enhancing catalyst stability.[26] The Cheng group demonstrated that in a phosphate-adsorbed NiFe LDH@Ni catalytic material system, phosphate can act as an effective pH buffer. The HPO_4^{2-} formed during the reaction helps mitigate proton corrosion during water oxidation, preventing the loss of active sites.[119] Li *et al.* introduced a zwitterionic oxyanion, *N*1,*N*3-bis(carboxymethyl)-*N*1-(3-((carboxymethyl)dimethylammonio)propyl)-*N*1,*N*3,*N*3-trimethylpropane-1,3-diaminium (z-TCQ), into the interlayer of NiFe LDH through a two-step room temperature gradient immersion strategy, thereby incorporating both carboxyl groups and quaternary ammonium cationic groups ($C–N^+$) into the host structure and enabling precise regulation of the OER microenvironment.[118] The resulting z-NiFe catalyst exhibits distinct interfacial properties relative to pristine NiFe LDH, as illustrated in Fig. 7a. *In situ* Raman spectra analyses in Fig. 7b and c indicate that both materials initially possess an alkaline surface environment at open circuit potential, whereas under anodic polarization the surface of pristine NiFe LDH gradually becomes locally acidic, as reflected by the increasing dominance of HCO_3^- over CO_3^{2-}. By contrast, z-NiFe maintains a CO_3^{2-} dominated surface environment across the whole potential range, indicating that the zwitterionic modification helps preserve a stable alkaline microenvironment during OER. This interpretation is further supported by the OH^- conductivity data in Fig. 7d, which reveal faster hydroxide transport in z-NiFe than in NiFe LDH. Such microenvironment regulation not only promotes reaction kinetics but also suppresses the dissolution of active metal species. Consistent with this trend, inductively coupled plasma mass spectrometry (ICP-MS) in Fig. 7e analysis after stability testing detected much lower Ni and Fe leaching from z-NiFe, suggesting that the maintained alkaline interface effectively mitigates acid induced corrosion of the catalytic surface. Overall, this approach indicates that zwitterionic intercalation can simultaneously stabilize the local reaction microenvironment and inhibit catalyst dissolution, thereby enabling concurrent improvement in OER activity and stability.

It is worth noting incidentally that this microenvironment modulation strategy also has profound applications in the counterpart reaction of the OER, the HER, particularly in the field of seawater electrolysis. Untreated natural seawater (pH 8.2 to 8.3) lacks sufficient buffering capacity. During the HER, the pH at the cathode surface increases sharply with rising current density. When the local pH reaches approximately 9.5 or higher, precipitates such as $Mg(OH)_2$ and $Ca(OH)_2$ form *in situ* near the cathode. These precipitates readily block the cathode surface, leading to catalyst deactivation and deteriorating the hydrogen evolution performance.[120–123] Although constructing a local acidic microenvironment at the active sites during reactant adsorption and product desorption is unsustainable for the OER, as discussed previously, for HER, building such a local acidic microenvironment on the catalyst surface *in situ* can hinder the formation of insoluble precipitates during natural seawater electrolysis. This facilitates dynamic HER and enhances both the activity and stability

 This journal is © The Royal Society of Chemistry 2026

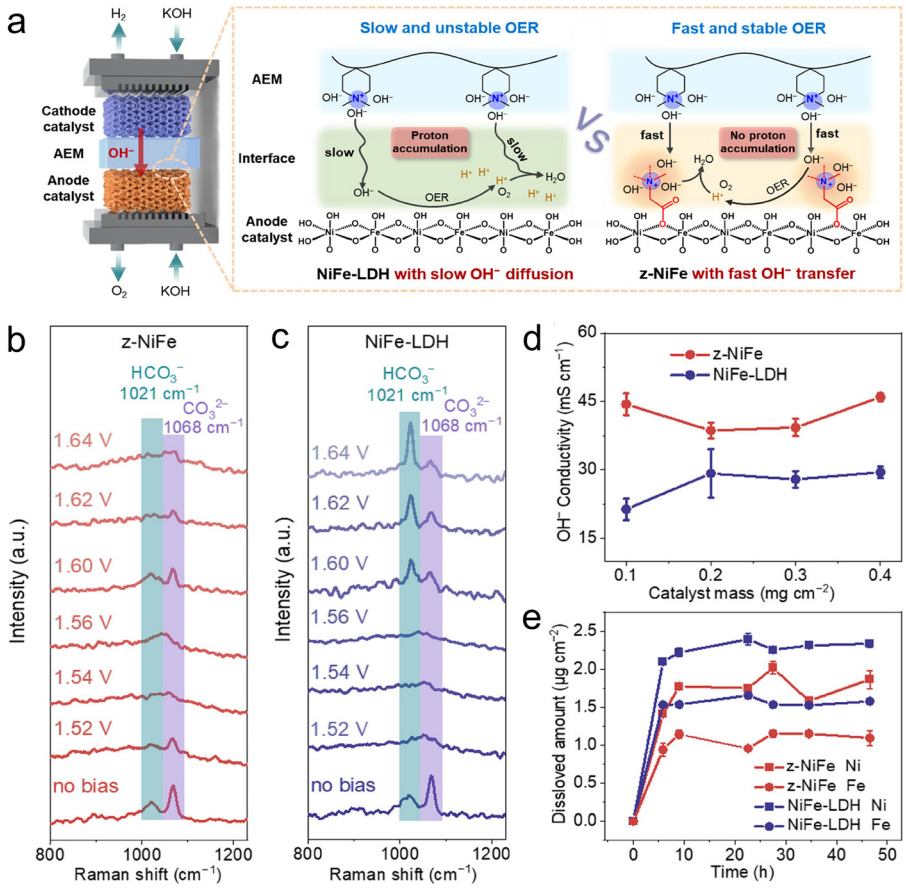

Fig. 7 (a) The introduction of quaternary ammonium cations significantly enhances OH^- transfer across the AEM–anode catalyst interface and creates a locally alkaline-enriched microenvironment around the metal active sites. *In situ* Raman spectra of (b) z-NiFe and (c) NiFe LDH in mixed solutions of $KHCO_3$ and K_2CO_3. (d) OH^- conductivity of z-NiFe and NiFe LDH at different catalyst masses. (e) ICP-MS for z-NiFe and NiFe LDH during the short-term stability at 100 mA cm^{-2}.[118] Reproduced with permission. Copyright 2025, John Wiley and Sons.

of the catalyst.[124–126] Bao's team introduced the oxyanion WO_4^{2-} as a precursor into a noble metal Pt catalytic system to construct a hybrid electrocatalyst. The H_xWO_y species formed during the reaction can act as a "proton sponge", enabling the dynamic storage and supply of H^+.[124] XRD characterization results revealed no phases related to precipitates in the system, confirming the successful construction of a local acid-like environment.

4 Oxyanions for adsorption optimization

4.1 Refining adsorption energetics for intermediates

From a thermodynamic perspective, optimizing and facilitating the effective adsorption of various oxygen-containing intermediates (such as *OH, *O and *OOH) at catalytic sites during the reaction represents a significant rationale for the introduction of oxyanions. Previous studies have established that regardless of the binding energy of the *O intermediate on the catalytic surface, there exists a constant difference of approximately 3.2 eV between the adsorption energies of the two key intermediates, *OOH and *OH.[127,128] This quantitative relationship, $\Delta G_{*OOH} - \Delta G_{*OH} = 3.2$ eV, implies that on the surfaces of most catalysts, the difference in adsorption energies between *OOH and *OH remains largely constant and cannot be independently tuned. This positive correlation scaling relationship is an intrinsic feature of the OER mechanism (particularly for the AEM) and directly imposes a theoretical minimum overpotential for OER, making it difficult to fall below 0.37 V.[87,129] Therefore, breaking this inherent scaling relationship is a key challenge for enhancing OER catalytic performance and overcoming the bottleneck of catalytic efficiency. The strategies for breaking this scaling relationship introduced in this review can be broadly categorized into two types. One involves activating the LOM (see Section 5) to circumvent the limitations of the AEM and avoid the constraints of the scaling relationship by altering the reaction pathway. The other involves introducing oxyanions to break the traditional scaling relationship through means such as electronic structure modulation, hydrogen bonding regulation, and defect engineering, thereby reducing OER overpotential.[87,130–132] In 2021, Xue *et al.* employed attenuated total reflectance surface-enhanced infrared absorption spectroscopy (ATR-SEIRAS) to

investigate the binding energies of oxygen-containing intermediates on the surfaces of three catalysts: RuO_2, S-RuO_2 and S-$RuFeO_x$.[133] The study found that compared to the pristine RuO_2 catalyst, the spectral bands corresponding to the *OO intermediate on S-RuO_2 and S-$RuFeO_x$ exhibited a red shift, with the *OO peak positions for S-RuO_2 and S-$RuFeO_x$ being similar. This phenomenon indicates that the doping of SO_4^{2-} can reduce the binding energy of *OO–H intermediates on the catalyst surface, and this modulatory effect is primarily attributable to the introduction of SO_4^{2-}, providing direct experimental evidence for the role of oxyanions in modulating intermediate adsorption. Research by Zhang *et al.* involved introducing SO_4^{2-} onto the surface of a Co_3O_4 catalyst to construct electrophilic acidic sites.[134] Due to the smaller steric hindrance of the *OH intermediate, SO_4^{2-} struggles to form effective hydrogen bonding interactions with the catalyst surface. In contrast, the H atom within the *OOH intermediate can form stable hydrogen bonds with SO_4^{2-}, thereby participating in the microscopic processes of the OER, significantly promoting the deprotonation step of the intermediate, and ultimately breaking the adsorption energy scaling relationship between *OOH and *OH. The core of this mechanism lies in the fact that oxyanions adsorbed on the catalyst surface can act as secondary binding sites. Leveraging differences in geometric configuration, they form hydrogen bonding interactions of varying strengths with *OOH and *OH intermediates, thereby disrupting the positive correlation between the adsorption energies of these two species. Research by Liao *et al.* has also corroborated this viewpoint.[81]

The introduction of oxyanions can also modulate the electronic structure of the catalyst, thereby optimizing the adsorption characteristics of OER intermediates. Multiple studies employing DFT calculations have demonstrated that oxyanions adsorbed on the catalyst surface can effectively increase the density of states at the Fermi level of the metal active centres and induce a shift in the metal d-band centre, consequently optimizing the adsorption energy of OER intermediates and lowering the reaction energy barrier.[135,136] Li *et al.* used density of states (DOS) analysis to reveal that phosphate incorporation can effectively tune the electronic structure of reconstructed oxyhydroxides.[65] As indicated in Fig. 8a, the d band centre of the Ni site in Ni(Fe)OOH-V_O-PO_4 is shifted from −1.08 eV in the undoped Ni(Fe)OOH-V_O catalyst to −0.68 eV, bringing it closer to the Fermi level. According to d band centre theory, such a shift is favourable for regulating the adsorption strength of OER intermediates and thus provides a more suitable electronic basis for the reaction. The differential charge density results in Fig. 8b further suggest that the Ni sites adjacent to PO_4^{3-} exhibit obvious electron depletion, which is beneficial for strengthening the interaction with oxygenated intermediates. Consistent with this trend, the Gibbs free energy profile in Fig. 8c confirms that PO_4^{3-} introduction lowers the barrier of the rate determining step and accelerates OER kinetics. Similar electronic modulation has also been reported for sulfate containing systems. Jin *et al.* found from the DOS results in Fig. 8d and e that SO_4^{2-} modification shifts the d band centre of NiFeO from −2.988 eV to −3.383 eV, indicating that sulfate induced electronic redistribution can also optimize the adsorption behaviour of intermediates and facilitate charge transfer during the OER.[85] In line with this result, Wu *et al.* constructed a SO_4^{2-}-absorbed NiOOH catalyst through electrochemical reconstruction of Ni_3S_2/NF, and their calculations demonstrated that sulfate adsorption causes an upshift of the d-band centre, thereby

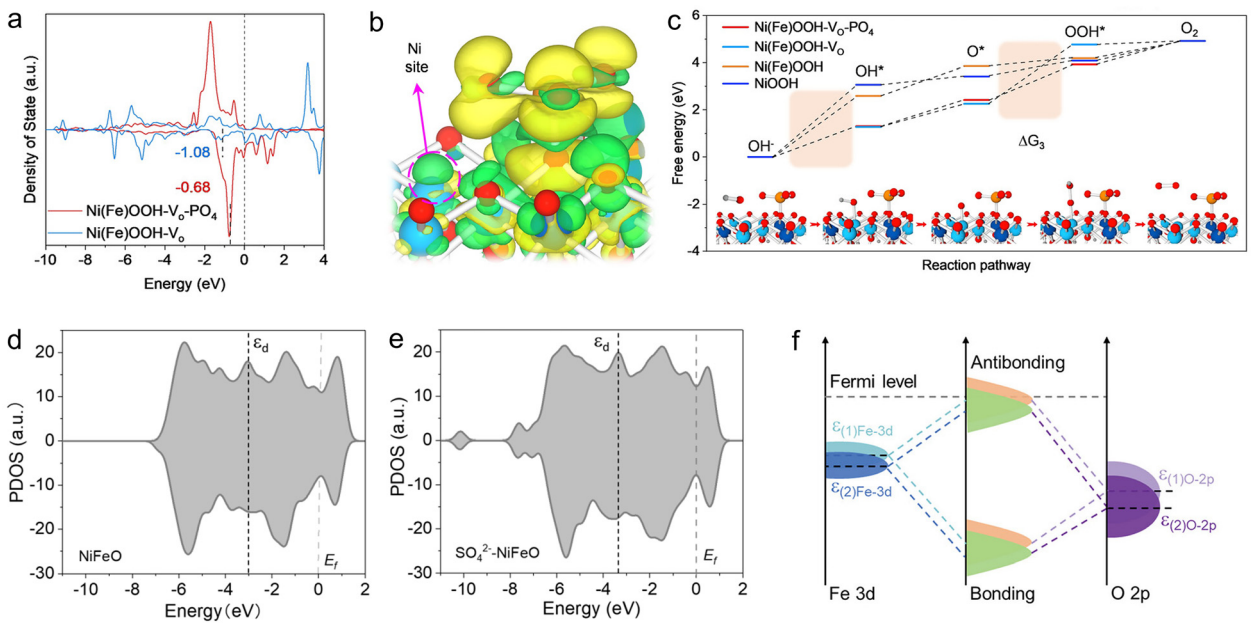

Fig. 8 (a) Density of states (DOS) of Ni 3d orbitals in Ni(Fe)OOH-V_O-PO_4 and Ni(Fe)OOH-V_O, respectively. (b) Differential charge densities of Ni(Fe)OOH-V_O-PO_4. Yellow and green contours represent electron accumulation and depletion, respectively. (c) Gibbs free energy profiles along the reaction pathway.[65] Reproduced with permission. Copyright 2020, John Wiley and Sons. The calculated DOS of (d) NiFeO and (e) SO_4^{2-}-NiFeO. (f) Orbital interaction between Fe 3d and O 2p.[85] Reproduced with permission. Copyright 2024, John Wiley and Sons.

This journal is © The Royal Society of Chemistry 2026

enhancing intermediate adsorption and lowering the energy barrier for the conversion of *OH to *O.[137] Luo *et al.* further reported a Co(Ni)OOH catalyst co-adsorbed with PO_4^{3-} and SO_4^{2-}, in which the d-band centre shifts from −1.73 eV to −1.12 eV after oxyanion modification.[138] This change in the electronic structure improves the adsorption strength of oxygen containing intermediates and ultimately promotes OER activity. Taken together, these studies indicate that surface or interfacial oxyanions can serve as effective electronic regulators by tuning the d-band centre and local charge distribution of active sites, thereby optimizing intermediate binding and improving OER performance.

The regulatory effects of oxyanions on OER performance are rarely governed by a single pathway. Instead, multiple mechanisms often operate cooperatively to deliver the overall catalytic enhancement. In 2023, Wang *et al.* introduced SO_4^{2-} onto the surface of an amorphous transition metal oxide, $ZnCo_xNi_yO_z$, through a two-step proton etching and ion exchange strategy, and systematically examined its role in OER modulation.[73] To clarify the underlying mechanism, they selected the reconstructed CoOOH surface as the representative model and established a CoOOH–SO_4 structure for DFT analysis. As illustrated in Fig. 9a, the adsorption configurations of the key OER intermediates, including *OH, *O, and *OOH, were optimized on both CoOOH and CoOOH–SO_4 surfaces, allowing a direct comparison of how adsorbed sulfate affects intermediate binding and surface reaction geometry. The electronic structure analysis in Fig. 9b further indicates that the pristine CoOOH surface shows a relatively limited contribution of Co 3d states near the Fermi level, implying comparatively weak electronic coupling between the Co active sites and the reaction intermediates. After sulfate adsorption, the Co 3d contribution around the Fermi level becomes markedly enhanced, suggesting that SO_4^{2-} modifies the local electronic environment of Co and improves interfacial electron transfer during OER. This electronic modulation is also reflected in the free energy profiles. According to Fig. 9c, sulfate adsorption selectively stabilizes the *OOH intermediate while exerting little influence on *OH adsorption, thereby weakening the conventional scaling relationship between *OH and *OOH. Such a combined effect, involving both electronic structure regulation and intermediate specific stabilization, provides a plausible origin for the enhanced OER activity of the catalyst.

In the preceding discussion within this section, we primarily focused on how oxyanions modulate the d-band centre of metal sites in the active MOOH phase (including both *in situ* synthesized and reconstruction derived MOOH). The core objective of this modulation is to optimize the adsorption energy of reaction intermediates. However, it must be emphasized that this electronic regulatory effect is not confined solely to the reconstructed active phase. Before the structural degradation and reconstruction of the pre-catalyst, oxyanions also play a crucial role in modulating the d-band of the metal centres. Research by Zhou *et al.* demonstrated that in borate modified NiFe-LDH nanosheets (f-NiFe-LDH-B), the borate anion can induce a shift in the d-band centre of the Ni sites prior to the structural degradation of NiFe-LDH.[139] This early-stage evolution of the electronic structure facilitates the reconstruction of the pre-catalyst into a highly active phase. Thus, it is evident that the modulation of the electronic structure by oxyanions is a dynamic process that persists throughout the entire evolutionary lifecycle of the catalyst. Recognizing this dynamic nature is of profound significance for the rational design of highly efficient electrocatalysts in the future.

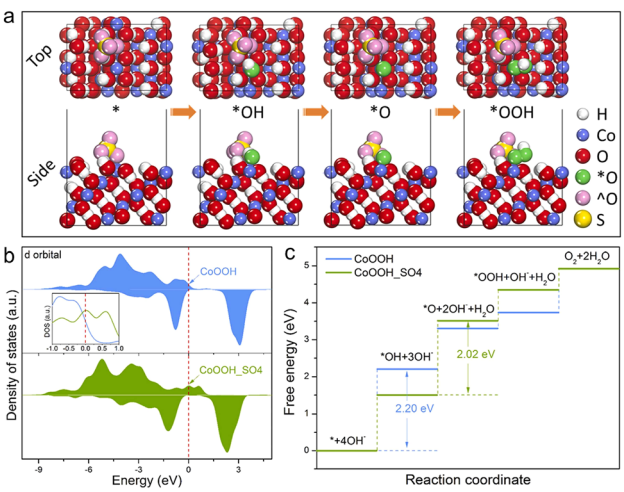

Fig. 9 (a) Optimized structural models of CoOOH–SO_4 for different OER steps. White balls represent hydrogen atoms, blue balls represent cobalt atoms, yellow balls stand for sulfur atoms, red balls represent the oxygen in the catalyst structure, green balls represent the oxygen adsorbed on the intermediate, and pink balls represent oxygen on the sulfate group. (b) DOS of CoOOH and CoOOH–SO_4 regarding the Co 3d orbitals. (c) Gibbs free energy diagrams of OER intermediates over CoOOH and CoOOH–SO_4.[73] Reproduced with permission. Copyright 2023, Elsevier.

4.2 Altering the RDS

Owing to their strong ability to regulate the electronic structure of active sites, oxyanions can not only lower the activation barrier of the rate determining step in the OER, but also alter the reaction pathway by inducing a shift in the rate determining step itself. Shao *et al.* reported that NiFeMo/NM can be *in situ* converted into γ-(Ni,Fe)–OOH decorated with adsorbed MoO_4^{2-}, and DFT results in Fig. 10a suggest that this modification shifts the rate determining step from *OH to *O toward *O to *OOH formation.[140] Meanwhile, the calculated overpotential decreases from 0.58 V to 0.40 V, indicating a substantial improvement in OER kinetics. This type of kinetic transition is also consistent with changes in Tafel behaviour. In 2019, Nørskov and co-workers proposed that a Tafel slope of about 39 mV dec^{-1} is characteristic of OER systems in which *OOH formation becomes the rate determining step (Fig. 10b).[141] In line with this analysis, Xue *et al.* found that pristine RuO_2 exhibits a Tafel slope of 69 mV dec^{-1}, whereas sulfate modification lowers this value to 49 mV dec^{-1}, bringing it closer to the characteristic range associated with a shifted rate determining step.[133] This interpretation was further supported by their later work in 2023.[142] A similar effect was also observed in molecular catalysts. Liu *et al.* introduced axial phosphate

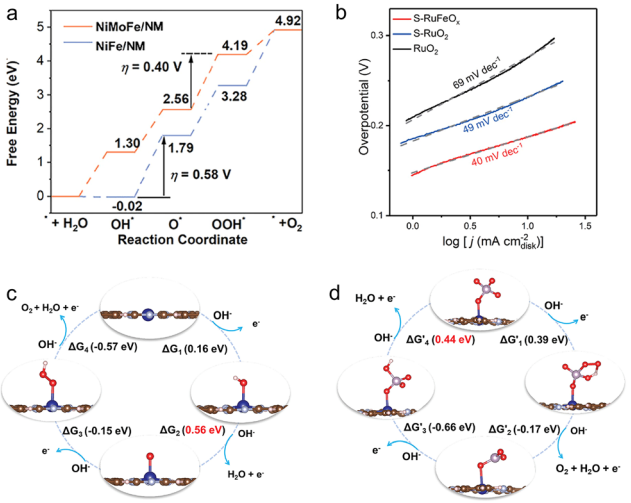

Fig. 10 (a) Gibbs free energy diagram of the OER on NiMoFe/NM and NiFe/NM.[140] Reproduced with permission. Copyright 2023, John Wiley and Sons. (b) Tefel plots of S-RuFeO$_x$, S-RuO$_2$, and commercial RuO$_2$.[133] Reproduced with permission. Copyright 2021, John Wiley and Sons. (c) The free energy change of the OER process over CoPc at 1.23 V *versus* RHE and (d) the free energy change of the OER process over PO$_4$-CoPc at 1.23 V *versus* RHE. The blue, mauve, bluish, brown, red, and white spheres represent Co, P, N, C, O, and H, respectively.[143] Reproduced with permission. Copyright 2022, John Wiley and Sons.

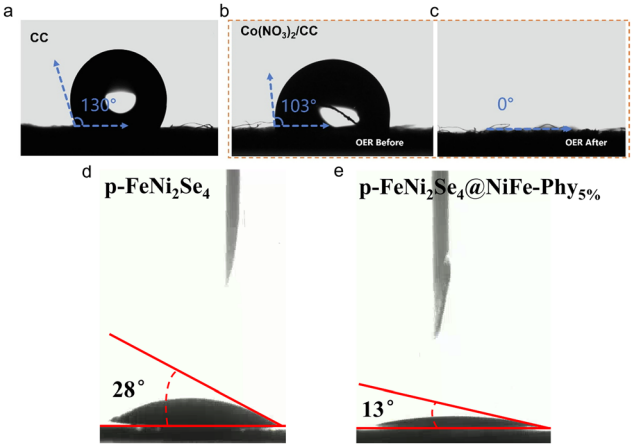

Fig. 11 Contact angle evaluation of the electrode surfaces of (a) carbon cloth (CC) and (b) and (c) Co(NO$_3$)$_2$/CC before (b) and after (c) OER electrochemical reconstruction.[145] Reproduced with permission. Copyright 2025, Elsevier. Contact angle measurements of (d) p-FeNi$_2$Se$_4$ and (e) p-FeNi$_2$Se$_4$@NiFe-Phy$_{5\%}$.[149] Reproduced with permission. Copyright 2024, John Wiley and Sons.

(PO$_4$) coordination into cobalt phthalocyanine (CoPc) supported on carbon nanotubes, and the results in Fig. 10c and d indicate that phosphate coordination changes the OER pathway by switching the rate determining step to the dehydrogenation of the HPO$_4$-Co$_1$N$_4$ intermediate.[143] At the same time, the Gibbs free energy change of this step decreases to 0.44 eV, which is lower than that of the original rate determining step before modification. Taken together, these studies demonstrate that oxyanions can actively regulate the kinetic bottleneck of the OER, not only by lowering the energy barrier of the rate determining step, but also by shifting the rate determining step itself.

4.3 Improving hydrophilicity of catalysts

Furthermore, the introduction of oxyanions can not only enhance the adsorption capacity of the pristine catalyst for oxygen-containing intermediates but also significantly improve the hydrophilicity of the catalyst, thereby optimizing OER kinetics.[94,144] Gan *et al.* reported that NO_3^- adsorption on reconstructed CoOOH can markedly improve the surface wettability of the catalyst.[145] As reflected by the contact angle measurements in Fig. 11a–c, the reconstructed CoOOH–NO_3^-/CC catalyst exhibits an almost zero contact angle, indicating extremely strong hydrophilicity. This behaviour is attributed to the presence of surface adsorbed oxyanions, which promotes the formation of hydrophilic surface species and thus enhances the affinity of the catalyst for the electrolyte. Improved hydrophilicity is beneficial for the timely release of evolved O_2 bubbles, preventing blockage of active sites, while also facilitating the transport of OH^- to the catalytic interface. A similar effect was reported by Zhang *et al.* in 2024 for a core–shell FeNi$_2$Se$_4$@NiFe-Phy catalyst prepared by surface etching. During the OER, this material undergoes *in situ* reconstruction to form a NiFeOOH active layer enriched with PO_4^{3-} and CO_3^{2-} derived from the *in situ* conversion of phytic acid.[146] According to the contact angle results in Fig. 11d and e, the introduction of the oxyanion layer reduces the contact angle from 28° for p-FeNi$_2$Se$_4$ to 13° for p-FeNi$_2$Se$_4$@NiFe-Phy$_{5\%}$, indicating a clear enhancement in hydrophilicity. These results suggest that surface oxyanions can improve interfacial wettability, thereby promoting gas release and reactant transport during the OER.

5 Oxyanions for lattice activation and stabilization

The AEM has long been recognized as the primary reaction pathway for the OER.[147] The AEM posits that the OER proceeds through a sequence of concerted electron–proton transfer steps on transition metal active centres at the catalyst surface. Adsorbed oxygen-containing intermediates (*OH, *O, and *OOH) undergo sequential transformation on these transition metal active sites, ultimately generating oxygen. The detailed reaction process is illustrated in Fig. 12.[148] In alkaline electrolytic environments, the detailed reaction steps for the AEM are as follows:

$$\text{Step 1: } H_2O + * \rightarrow OH^* + H^+ + e^-$$

$$\text{Step 2: } OH^* \rightarrow O^* + H^* + e^-$$

$$\text{Step 3: } H_2O + O^* \rightarrow OOH^* + H^+ + e^-$$

$$\text{Step 4: } OOH^* \rightarrow O_2^* + H^+ + e^-$$

This journal is © The Royal Society of Chemistry 2026

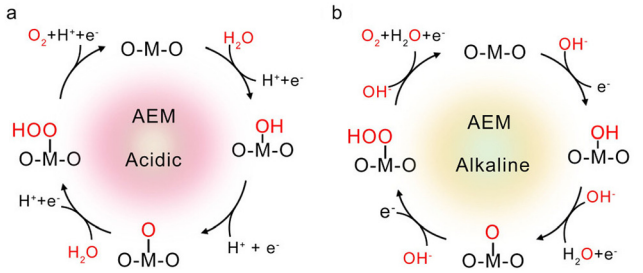

Fig. 12 Simplified AEM pathways of the OER in acidic (a) and alkaline (b) environments. Chemically inert lattice oxygen and oxygen in the electrolyte are marked in black and red, respectively.[155] Reproduced with permission. Copyright 2025, Elsevier.

$$\text{Step 5: } O_2^* \rightarrow O_2 + *$$

$$\text{Overall: } 2H_2O \rightarrow 4H^+ + O_2 + 4e^-$$

It is evident from this that under the AEM pathway, the OER occurs exclusively at the metal active sites on the catalyst surface, and the oxygen atoms are derived entirely from the electrolyte. However, as discussed in Section 4, the AEM pathway is fundamentally limited by the scaling relationship between the adsorption energies of surface intermediates. This intrinsic constraint sets the theoretical OER overpotential at about 0.37 V, thereby limiting further improvement in intrinsic catalytic activity and creating a major challenge for the design and practical application of high performance OER catalysts.

In recent years, the LOM has been substantiated by numerous studies as an effective pathway to circumvent the aforementioned scaling relationship and overcome the thermodynamic limitations of the AEM.[150–154] This advantage stems from the unique reaction pathway of the LOM. In contrast to the AEM, the LOM proposes that lattice oxygen atoms within the catalyst's crystal structure can directly participate in the formation of oxygen molecules. In other words, oxygen atoms from the lattice not only serve as structural supports within the catalyst framework but also act as active species directly involved in the OER. Fig. 13 illustrates three types of LOM pathways characterized by different active site configurations: the oxygen vacancy site mechanism (OVSM), the single-metal site mechanism (SMSM), and the dual-metal site mechanism (DMSM). Despite the differences in the nature of the active sites, the fundamental reaction steps of the LOM can be uniformly summarized into the following four stages. The first step is lattice oxygen activation. Driven by the applied anodic potential, the covalency of the M–O bonds between metal sites and bridging oxygen atoms on the catalyst surface is significantly enhanced. Oxygen ligands undergo partial oxidation and lose electrons, forming highly electrophilic reactive oxygen species. The second step involves a nucleophilic attack reaction. OH^- or H_2O molecules from the electrolyte, acting as nucleophiles, directionally attack the activated lattice oxygen sites. Through nucleophilic addition and elimination processes, a key O_2^- intermediate is formed. This step is central to O–O bond formation in the LOM. The third step is the

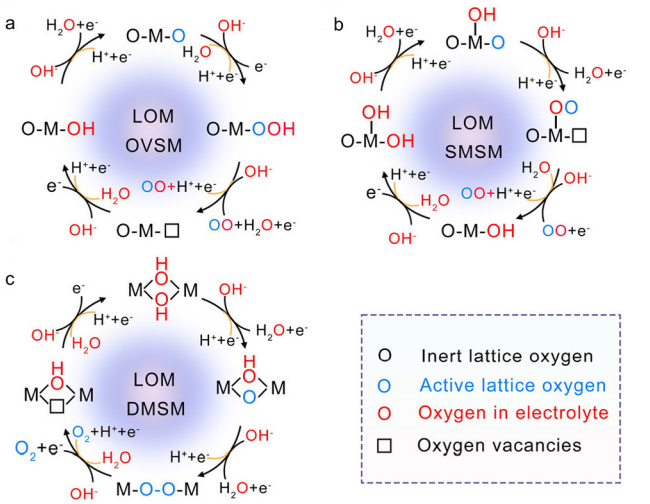

Fig. 13 Several typical LOM pathways involving different sites of OER in acidic and alkaline media. (a) Oxygen vacancy site mechanism (OVSM), (b) single metal site mechanism (SMSM), and (c) dual-metal-site mechanism (DMSM).[155] Reproduced with permission. Copyright 2025, Elsevier.

formation of an oxygen vacancy. In this stage, the superoxide-like O_2^- intermediate further desorbs, releasing an O_2 molecule. This results in the loss of lattice oxygen from the catalyst surface, thereby creating highly reactive oxygen vacancies. These vacancies can serve as active sites for subsequent reactions, accelerating the catalytic cycle. The fourth step is vacancy filling. OH^- or H_2O molecules from the electrolyte act as oxygen sources, rapidly replenishing the formed oxygen vacancies and restoring the catalyst surface structure to its initial state, thus completing a full catalytic cycle. Precisely because the LOM bypasses the formation of the high-energy-barrier *OOH intermediate required in the AEM, it thermodynamically avoids the constraints of the AEM scaling relationship, enhances the intrinsic activity of the catalyst, and consequently provides a viable pathway for achieving the OER at lower overpotentials.[156]

A growing number of studies have demonstrated, through approaches such as Tafel slope analysis, chemical probe experiments, and theoretical calculations, that the incorporation of oxyanions can promote the lattice oxygen mechanism and thereby improve OER performance.[25,157] For example, Wang *et al.* used tetramethylammonium hydroxide (TMAOH) as a chemical probe in place of KOH. By taking advantage of the electrostatic interaction between negatively charged $O^{2\delta-}$ species and TMA^+ cations, they were able to identify the $O^{2\delta-}$ intermediates formed during the OER, thus providing direct evidence for the involvement of the lattice oxygen mechanism, as presented in Fig. 14a and b.[158] Tao *et al.* further examined this issue by *in situ* differential electrochemical mass spectrometry (DEMS). Using ^{18}O labelled Fe-Ni_2P/$NiMoO_4$ in a $H_2{}^{16}O$ electrolyte, they detected a clear $^{16}O^{18}O$ signal during the OER, which confirms the participation of lattice oxygen in oxygen evolution, as indicated in Fig. 14c.[159] Cabot *et al.* combined experimental observations with theoretical analysis to show that SO_4^{2-} introduction is a key factor driving the transition

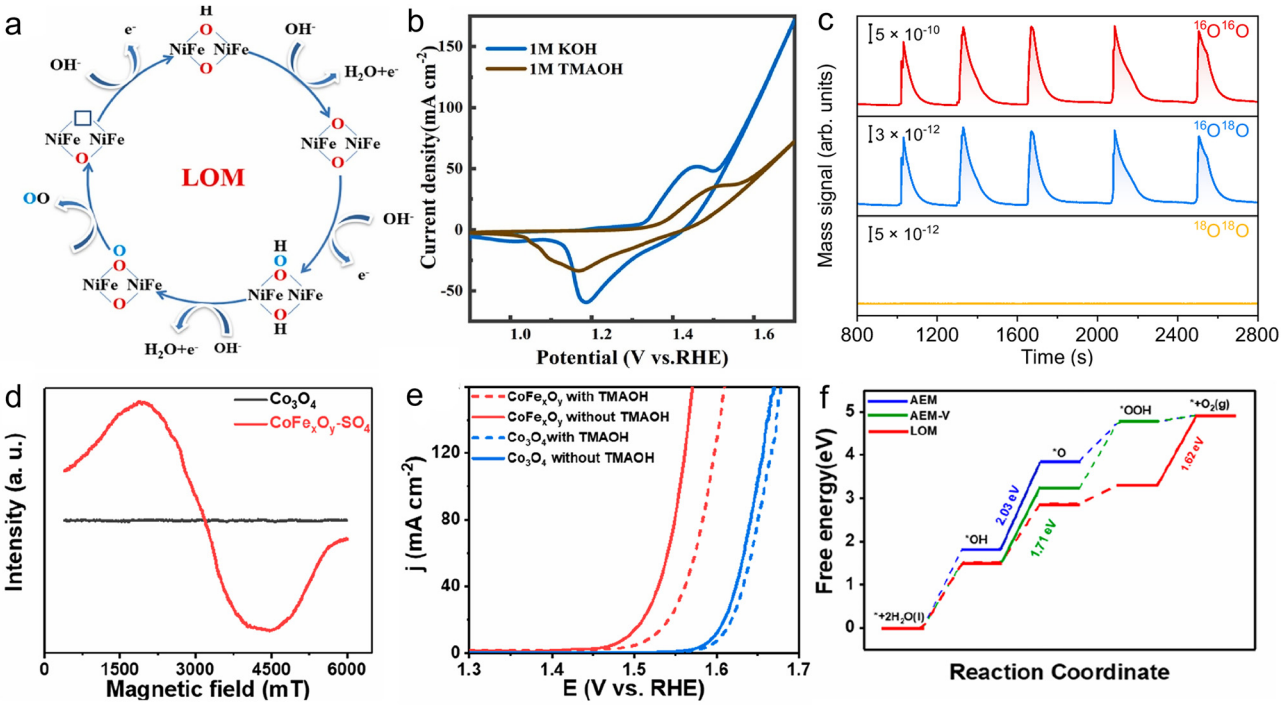

Fig. 14 (a) Schematic diagram of the LOM. (b) LSV curves of Ni_3S_2 and NiFeOOH-SO_4/Ni_3S_2/NF in 1 M TMAOH.[158] Reproduced with permission. Copyright 2025, Elsevier. (c) *In situ* DEMS signals of Fe-Ni_2P/$NiMoO_4$ for $^{16}O^{16}O$, $^{16}O^{18}O$, and $^{18}O^{18}O$ related to testing time.[159] Reproduced with permission. Copyright 2025, Springer Nature. (d) EPR spectra of $CoFe_xO_y$–SO_4-200 and Co_3O_4. (e) OER polarization of $CoFe_xO_y$–SO_4-200 and Co_3O_4 in 1 M KOH with and without TMAOH. (f) Free energies of OER steps in both mechanisms on $CoFeO_2$ with perfect surface and $CoFeO_2$ with oxygen vacancies.[175] Reproduced with permission. Copyright 2023, American Chemical Society.

of $CoFe_xO_y$-SO_4 from the AEM to LOM. As reflected in Fig. 14d, the electron paramagnetic resonance (EPR) signal associated with oxygen vacancies at $g = 2.12$ is much stronger for $CoFe_xO_y$–SO_4 than for SO_4^{2-}-free Co_3O_4, suggesting that SO_4^{2-} promotes the generation of oxygen vacancies and thereby provides a structural basis for LOM activation. This conclusion is further supported by the chemical probe results in Fig. 14e. After TMA^+ was introduced into the electrolyte, the OER activity of $CoFe_xO_y$–SO_4 decreased markedly, whereas Co_3O_4 showed little change, indicating that the SO_4^{2-} modified catalyst mainly follows the lattice oxygen mechanism. In addition, DFT calculations reveal that after oxygen vacancies are introduced into $CoFeO_2$, the free energy barrier of the rate determining step becomes lower for the LOM than for the AEM, as summarized in Fig. 14f. These results further support the view that SO_4^{2-} induced oxygen vacancies thermodynamically favour LOM activation.

5.1 Promoting M–O covalency for lattice oxygen activation

Regulating the covalency of metal–oxygen (M–O) bonds is crucial for triggering the LOM.[160–163] During the OER catalytic process, the strength of M–O covalent bonds determines the reactivity of lattice oxygen.[164] As discussed above, stronger M–O covalency reflects a greater overlap between metal d orbitals and O 2p orbitals, which can shift the O 2p band closer to the Fermi level. This electronic reconstruction lowers the charge transfer energy between metal and oxygen, facilitates oxygen vacancy formation, and enhances the redox activity of lattice oxygen, thereby promoting its direct participation in OER.[165,166] In this context, oxyanion introduction has attracted increasing attention as an effective approach for enhancing M–O covalency and triggering the LOM. For example, SeO_3^{2-}, owing to its lone pair electrons, can readily adsorb on transition metal oxide surfaces and strengthen the covalent interaction between metal centres and oxygen ligands.[167–169] In 2023, Zhang *et al.* reported that a combined strategy of *in situ* SO_4^{2-} modification and oxygen vacancy engineering can reinforce M–O covalency in inverse spinel $NiFe_2O_4$, leading to markedly improved OER activity.[170] More direct evidence was later provided by Liu *et al.*, who developed a SeO_4^{2-} intercalated NiFeOOH catalyst, denoted as NiFeOOH–SeO.[71] They proposed that SeO_4^{2-} intercalation broadens the Ni e_g^* orbital, raises the O 2p energy level, and promotes electron transfer from Ni to Fe, thereby driving the formation of high valence Ni species. These effects collectively increase the reactivity of lattice oxygen and facilitate oxygen vacancy generation. As a result, SeO_4^{2-} effectively activates lattice oxygen through enhanced Ni O covalency, making the OER pathway more favourable toward the LOM.

5.2 Balancing activation and regeneration for stability

Although the LOM can markedly improve the intrinsic OER activity of catalysts, it is often accompanied by irreversible lattice oxygen loss and dissolution of redox active metal centres, which eventually causes structural degradation and

 This journal is © The Royal Society of Chemistry 2026

performance decay.[171] Previous studies have shown that LOM activation often comes at the expense of long-term durability, because repeated lattice oxygen redox and oxygen vacancy cycling can gradually disrupt the crystal framework and weaken catalytic stability.[115,116,172] Therefore, the key to developing efficient LOM based catalysts lies in the coordinated regulation of lattice oxygen activation and regeneration. At present, a common strategy is to introduce oxygen reservoir components that can dynamically compensate for oxygen vacancies formed during the OER, thereby stabilizing the lattice framework and suppressing metal dissolution. For example, Li *et al.* incorporated high valence oxophilic W into the $NiCo_2O_4$ spinel lattice and established an oxophilic site mediated dynamic oxygen replenishment mechanism.[173] Similarly, Hou's team proposed an oxygen pump strategy by introducing a Ni_4Mo alloy into NiFe LDH.[174] Owing to the strong oxophilicity of Ni_4Mo, OH^- can be efficiently captured from the alkaline electrolyte and transferred to the NiFe LDH component, thus replenishing lattice oxygen vacancies and promoting a dynamic balance between lattice oxygen release and regeneration. In addition to such oxygen reservoir design, heterostructure construction has also emerged as an effective route for coupling lattice oxygen activation with regeneration. Liu *et al.* developed a heterostructure in which amorphous NiFe LDH nanosheets encapsulate pyramidal $Fe_2(MoO_4)_3$(FeMoO).[152] This architecture not only introduces abundant oxygen vacancies but also generates an intrinsic interfacial electric field, which strengthens OH^- adsorption at the interface. The adsorbed OH^- can then refill oxygen vacancies generated during the LOM through nucleophilic attack, thereby enabling *in situ* lattice oxygen regeneration and suppressing the accumulation of oxygen vacancies and structural defects.

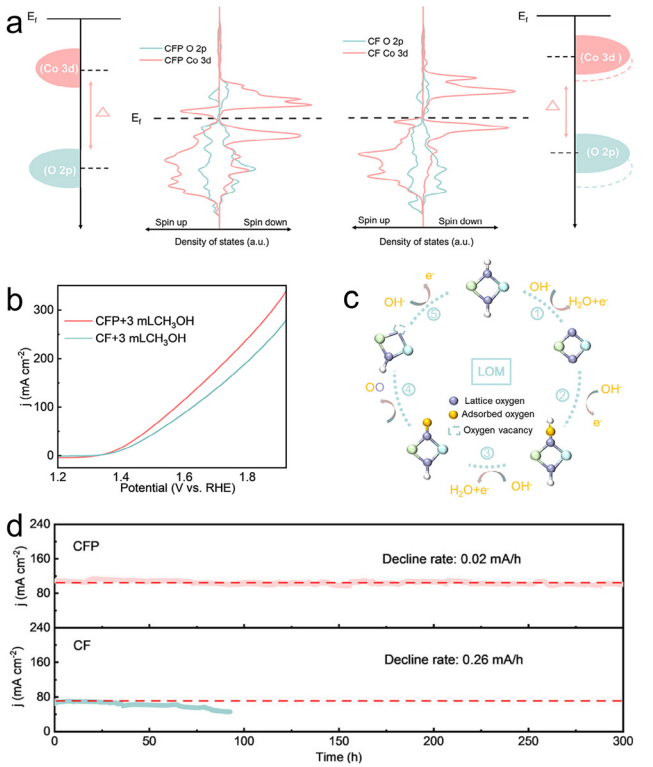

Fig. 15 (a) The schematic band diagrams and density of states of CF and CFP. (b) LSV curves of CF and CFP in 30 mL 1 M KOH + 3 mL CH_3OH. (c) Schematic illustration of the lattice oxygen mechanism. (d) Amperometric *i–t* curve test of CFP and CF at 1.633 V *versus* RHE without iR compensation.[176] Reproduced with permission. Copyright 2025, John Wiley and Sons.

Recent studies suggest that oxyanion introduction can also provide an effective route for balancing lattice oxygen activation and regeneration. On the one hand, the interaction between oxyanions and metal active sites can alter the bonding characteristics of M–O bonds, including bond elongation and enhanced covalency. In particular, the highly covalent central atoms of oxyanions exert a pronounced inductive effect, which enhances the covalency of M–O bonds, tunes the O 2p band centre, lowers the activation barrier for lattice oxygen, and thereby facilitates LOM activation. On the other hand, oxyanion modification can promote the *in situ* formation of highly active MOOH phases during the OER, which improves the adsorption kinetics and uptake of OH^-. At the same time, modulation of the metal d band centre further optimizes the adsorption of OH^- and other oxygen containing intermediates, enabling timely replenishment of lattice oxygen consumed during the LOM and supporting the establishment of a dynamic oxygen regeneration cycle. Through this dual function, oxyanions can help prevent excessive lattice oxygen loss and alleviate structural degradation during operation. In other words, for oxyanions to promote lattice oxygen participation without accelerating catalyst collapse, they are required to simultaneously and precisely modulate both the O 2p orbitals and the metal d orbitals, thereby establishing a dynamic equilibrium between the consumption and regeneration of lattice oxygen. Only when the OH^- in the electrolyte can be captured rapidly enough to fill the newly generated oxygen vacancies, will the participation of lattice oxygen not evolve into irreversible lattice destruction. PO_4^{3-} provides a representative example of this type of regulation. He *et al.* prepared a porous layered PO_4^{3-}-modified CoFe oxide (CFP) nanosheet catalyst on nickel foam through electrodeposition and phosphorization.[176] According to Fig. 15a, PO_4^{3-} adsorption shifts the O 2p band centre upward toward the Fermi level and strengthens M–O orbital hybridization, and these changes together promote lattice oxygen activation and increase its participation in OER. Meanwhile, phosphate adsorption also induces an upshift of the Co 3d band centre, which is favourable for faster OH^- adsorption on the catalyst surface. The methanol oxidation results in Fig. 15b further indicate that the phosphate modified CFP catalyst exhibits a higher current response than the phosphate-free counterpart, suggesting a stronger OH^- adsorption capability. Such rapid OH^- uptake is beneficial for compensating the lattice oxygen consumed at the initial stage of the reaction, thereby helping maintain a dynamic balance between lattice oxygen activation and regeneration. This rapid OH^- adsorption can compensate for the consumed lattice oxygen and ensure the stable LOM cycle (Fig. 15c). Stability

test results indicate that CFP exhibits an OER stability of over 300 h at a current density of 100 mA cm^{-2}, far outperforming the CF (Fig. 15d). In summary, this demonstrates that the lattice oxygen mediated cycling mechanism of the phosphate modified material is capable of maintaining long-term stability while ensuring excellent catalytic performance.

6 Oxyanions for other regulatory effects

6.1 Exposing internal active sites of LDHs

Electrocatalytic reactions are inherently surface processes occurring at the catalyst's surface/interface. The complex electron transfer and adsorption/desorption behaviours of intermediates involved in the OER are contingent upon specific active centres located on or near the catalyst surface region. Consequently, in the OER, a direct structure–activity relationship exists between the exposure degree of active sites and catalytic performance.[177] How to increase the number of available active sites within a catalyst to enhance its intrinsic catalytic activity has consistently been one of the key scientific questions garnering long-term attention in this field. Motivated by this, researchers continuously strive to develop efficient and stable OER electrocatalytic materials. An ideal catalyst necessitates concurrently meeting multiple requirements, such as exposing more active sites per unit geometric area, possessing faster electron transport capabilities, and achieving higher mass transfer efficiency, all aimed at reducing the OER overpotential.[8,178]

In recent years, the introduction of oxyanions has been widely confirmed to effectively expose ''hidden'' active sites within catalysts, an effect that is particularly pronounced in layered double hydroxide (LDH) systems, which possess unique two-dimensional lamellar structures. Existing research indicates that when oxyanions are present in an intercalated form, the host materials investigated are almost exclusively Fe/Co/Ni-based LDHs.[36] For LDH materials, the intercalation of large-sized oxyanions typically expands the interlayer spacing of these layered materials. This, in turn, endows the material with a larger specific surface area, exposing metal active sites within the layers, while simultaneously enhancing electrolyte permeability and mass transport capability within the interlayer regions of the LDH, thereby boosting OER activity. Although some large-sized anions may be displaced by anions such as CO_3^{2-} from the solution during the reaction, the changes in material morphology and structure induced by intercalation still positively impact catalytic activity.[36,77,179–181] The expansion of LDH interlayer spacing is commonly verified through XRD characterization. According to Bragg's law ($2d \sin\theta = n\lambda$, where d represents the interplanar spacing, θ represents the diffraction angle, n represents the order of diffraction, and λ represents the X-ray wavelength), under fixed conditions of λ and n, if the interlayer spacing d increases, the corresponding θ value decreases. Liu *et al.* synthesized carboxylate-intercalated 60CoNiFe LDH *via* a one-step hydrothermal method using $Co(CH_3COO)_2$ as the metal precursor.[157] As shown in Fig. 16a, with an increase in the amount of carboxylate doping, the diffraction angle corresponding to the LDH (003) crystal plane gradually decreases, confirming the layer expansion effect induced by carboxylate intercalation. The enlarged interlayer spacing is beneficial for exposing more active sites within the LDH framework. This structural advantage is further reflected in the interfacial charge transfer behaviour. According to the electrochemical impedance spectroscopy (EIS) results in Fig. 16b, CH_3COO^- doped 60CoNiFe LDH/NF exhibits a much lower charge transfer resistance than undoped NiFe LDH/NF, indicating that interlayer expansion can reduce mass transport resistance and facilitate interfacial electron transfer. Dong *et al.*, for the first time, leveraged the anion exchange properties of LDHs to prepare a NiFe LDH Seb catalyst *via* sebacate intercalation and achieved *in situ* borate anion exchange in a near-neutral borate electrolyte.[77] Given that CO_3^{2-} is an unavoidable intercalating anion during LDH synthesis and electrochemical testing, the authors systematically compared the structure and performance of a CO_3^{2-}-intercalated sample (NiFe LDH SebCOexc) with a borate-intercalated sample (NiFe LDH SebBOexc).[44] XRD results (Fig. 16c and d) showed that the interlayer spacing of the sample post-borate intercalation was larger than that of the sample with carbonate intercalation under the same conditions. Concurrently, electrochemically active surface area measurements indicated that, under identical conditions, the electrochemically active surface area of NiFe LDH SebBOexc was larger than that of NiFe LDH SebCOexc. This difference is attributed to the *in situ* exchange and intercalation of borate anions, which promote more sufficient exposure of the metal sites within the LDH layers, thereby enhancing the utilization efficiency of active sites (Fig. 16e). Related observations have also been reported for phosphate intercalation.[97] After PO_4^{3-} insertion into the NiFe LDH interlayer, the expanded gallery spacing improves electrolyte penetration and mass transport, while also making interlayer active sites more accessible, as reflected in Fig. 16f. In addition, phosphate intercalation changes the LDH morphology from relatively thick plate like particles to ultrathin nanosheets, as illustrated in Fig. 16g and h. This structural evolution suppresses particle agglomeration and further increases the exposure of surface-active sites. Taken together, these studies show that oxyanion intercalation can regulate both interlayer structure and catalyst morphology, thereby enhancing active site accessibility and improving reaction kinetics.

By the way, the introduction of oxygen-containing organic acid anions has also been confirmed to exhibit similar effects. He *et al.* incorporated citrate anions (CA) into NiFe LDH *via* a hydrothermal method.[182] XRD and Brunauer–Emmett–Teller (BET) characterization results showed that the interlayer spacing of the resulting NiFe LDH-CA2 sample was significantly enlarged compared to that without CA intercalation. This physical spatial expansion facilitates the exposure of active sites, the diffusion of the electrolyte, and the release of gas, thereby enhancing catalytic activity.

6.2 Inhibiting metal dissolution

The segregation phenomenon of active metal centres during the OER process is one of the common stability issues faced by

 This journal is © The Royal Society of Chemistry 2026

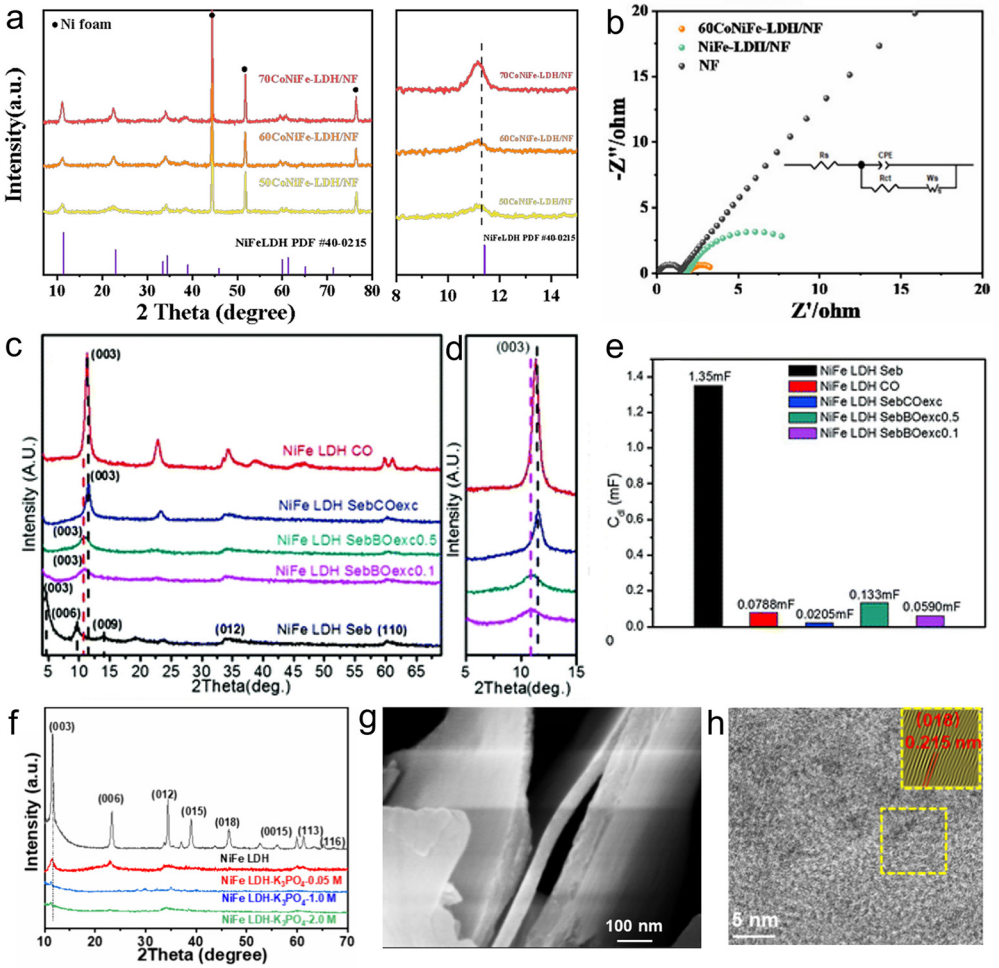

Fig. 16 (a) XRD patterns of 50CoNiFe LDH/NF, 60CoNiFe LDH/NF, and 70CoNiFe LDH/NF. (b) Nyquist plots of 60CoNiFe LDH/NF, NiFe LDH/NF, and NF.[157] Reproduced with permission. Copyright 2025, American Chemical Society. (c) XRD patterns of the NiFe LDH samples. (d) Amplified XRD patterns in the range of 5–15° showing the different (003) peak positions of carbonate NiFe LDHs (black dashed line) and borate NiFe LDHs (pink dashed line). (e) Double-layer capacitance C_{dl} of each sample obtained from the fitting of the Nyquist plots, which is proportional to the electrochemically active surface area (ECSA).[77] Reproduced with permission. Copyright 2019, Royal Society of Chemistry. (f) XRD patterns of pristine NiFe LDH and NiFe LDH-K_3PO_4-2.0 M. (g) High-magnification SEM images of NiFe LDH. (h) HRTEM image of NiFe LDH-K_3PO_4-2.0 M nanosheets.[97] Reproduced with permission. Copyright 2024, American Chemical Society.

transition metal-based electrocatalysts, often leading to the degradation of the catalyst structure.[39] As mentioned earlier, metal–oxygen covalency plays a crucial role in inhibiting metal segregation and enhancing catalyst stability. Research indicates that the introduction of oxyanions can enhance the M–O covalency in catalysts, implying an increase in M–O bond strength, thereby suppressing the loss of active metal. Wang *et al.* pointed out that specific oxyanions (such as PO_4^{3-} and NO_3^-) can inhibit metal leaching in transition metal hydroxide electrocatalysts during the OER and enhance structural stability by modulating the TM–O covalent bond and the TM-3d band centre.[183] Research by Zhang *et al.* showed that the introduction of adsorbed CO_3^{2-} can synergistically modulate the upshift of the O 2p orbital and the downshift of the Fe 3d orbital, reducing the charge transfer energy from the Fe 3d orbital to the O 2p orbital from 0.09 eV to −0.02 eV. This indicates that the adsorption of CO_3^{2-} on the catalyst surface significantly enhances the covalency of the Fe–O bond in NiFeOOH-CO_3^{2-}, thereby improving the stability of the Fe–O bond and reducing the leaching tendency of Fe atoms.[184]

Furthermore, the dissolution of active metal centres is often triggered by the irreversible loss of the lattice oxygen framework. In this context, oxyanions can act as structural stabilizers to effectively mitigate this degradation process. Taking the classic RuO_2 system as an example, during the acidic OER process, the poor stability of the anodic RuO_2 catalyst primarily stems from the over-oxidation of lattice oxygen, leading to the substantial formation of oxygen vacancies.[114,185] This exposes Ru atoms adjacent to the oxygen vacancies to the electrolyte, subjecting them to over-oxidation and ultimately resulting in the collapse of the RuO_2 crystal structure and significant leaching of the active metal Ru from the surface.[186] Xue *et al.* employed Ba to anchor SO_4^{2-}, forming coordination-saturated lattice oxygen, which effectively inhibited the formation of

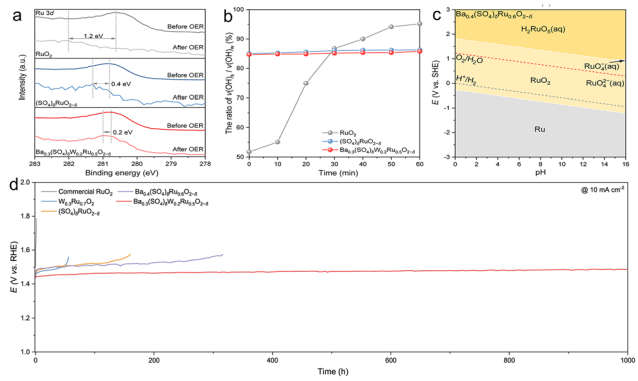

Fig. 17 (a) The intensity ratio of $\nu(OH)_s/\nu(OH)_w$ on RuO_2, $(SO_4)_\delta RuO_{2-\delta}$, and $Ba_{0.3}(SO_4)_\delta W_{0.2}Ru_{0.5}O_{2-\delta}$ over the course of 1 h acidic OER at 1.5 V. (b) High-resolution XPS spectra of Ru 3d for RuO_2, $(SO_4)_\delta RuO_{2-\delta}$, and $Ba_{0.3}(SO_4)_\delta W_{0.2}Ru_{0.5}O_{2-\delta}$ before and after OER. (c) Ru Pourbaix diagram for $Ba_{0.4}(SO_4)_\delta Ru_{0.6}O_{2-\delta}$ generated with an aqueous ion concentration of 10^{-6} M at 25 °C. (d) Chronopotentiogram of commercial RuO_2, $W_{0.3}Ru_{0.7}O_2$, $(SO_4)_\delta RuO_{2-\delta}$, $Ba_{0.4}(SO_4)_\delta Ru_{0.6}O_{2-\delta}$, and $Ba_{0.3}(SO_4)_\delta W_{0.2}Ru_{0.5}O_{2-\delta}$ at 10 mA cm^{-2} in 0.5 M H_2SO_4.[142] Reproduced with permission. Copyright 2023, Springer Nature.

oxygen vacancies on the RuO_2 surface and protected the lattice oxygen.[142] *In situ* attenuated total reflection surface-enhanced absorption spectroscopy (ATR-SEIRAS) indicated that in pristine RuO_2, the proportion of liquid water ($\nu(OH)_w$) formed by combining with lattice oxygen during the OER gradually decreased. In contrast, for $Ba_{0.3}(SO_4)_\delta W_{0.2}Ru_{0.5}O_{2-\delta}$ with anchored SO_4^{2-}, the proportion of $\nu(OH)_w$ remained stable, demonstrating that oxygen vacancies were not extensively formed and lattice oxygen was not over-oxidized (Fig. 17a). This stabilizing effect is further supported by the Ru 3d XPS spectra in Fig. 17b. After the OER, pristine RuO_2 exhibits a pronounced positive shift in Ru 3d binding energy, whereas the shift in the SO_4^{2-} anchored sample is much smaller, suggesting that SO_4^{2-} helps inhibit the dissolution of highly oxidized Ru species and maintain structural integrity. Consistent with these observations, the Pourbaix analysis in Fig. 17c indicates that RuO_2 transforms into soluble H_2RuO_5 at 1.32 V under acidic conditions, while the stability limit of $Ba_{0.4}(SO_4)_\delta Ru_{0.6}O_{2-\delta}$ extends to 1.83 V. The chronopotentiometry (CP) durability results demonstrate that sulfate anchoring significantly enhances the catalytic stability of the material. Specifically, the $Ba_{0.3}(SO_4)_\delta W_{0.2}Ru_{0.5}O_{2-\delta}$ material can robustly sustain the OER process for 1000 h at a constant current density of 10 mA cm^{-2} in 0.5 M H_2SO_4 (Fig. 17d). These results explicitly demonstrate that anchoring oxyanions prevents the structural breakdown of the catalyst, which is fundamentally essential for inhibiting active metal dissolution and improving the overall thermodynamic stability of the catalyst.

Additionally, NO_3^- has also been demonstrated to enhance the resistance of active metals against dissolution, thereby improving structural stability and OER activity. Liao *et al.* synthesized $FeOOH/Ni_3(NO_3)_2(OH)_4$ with lattice incorporated NO_3^-. By utilizing the strong chemical interaction between NO_3^- and Fe sites, they effectively suppressed Fe segregation during the OER process, enhancing the catalyst's stability under high potentials.[187] Gan *et al.* confirmed that NO_3^- can adsorb on the catalyst surface, forming an anionic protective layer that inhibits the dissolution and loss of metal active sites, consequently improving the stability of water electrolysis.[145]

6.3 Enhancing seawater OER performance

Finally, the introduction of oxyanions into the electrocatalysts can also suppress side reactions of the OER, particularly in seawater electrolysis systems. A key challenge for the large-scale application of seawater electrolysis lies in the presence of Cl^- in the electrolyte. It not only triggers the competitive chlorine oxidation reaction against OER but also leads to anode corrosion.[188] Research indicates that SO_4^{2-} adsorbed on the catalyst anode surface can block interfering anions like Cl^- through electrostatic repulsion, thereby inhibiting side reactions and anode corrosion.[189–191] Intercalated SO_4^{2-} in LDHs has also been confirmed to possess this repulsive effect.[192] Phosphates on the catalyst surface similarly exhibit excellent chloride ion repulsion capabilities, enhancing the corrosion resistance and selectivity of catalysts in seawater OER systems.[119,149,193–195] Analogously, anions such as MoO_4^{2-}, $C_2O_4^{2-}$, and CrO_4^{2-} have also been reported to possess the same function.[84,140,196,197]

7 Summary and outlook

In summary, the roles of oxyanions in OER electrocatalysis have far exceeded the scope of mere electronic structure modulation, demonstrating multi-dimensional functionalities ranging from dynamic reconstruction to reaction pathway regulation. Firstly, the controlled sacrifice of oxyanions effectively induces deep reconstruction of the catalyst, forming high-valence metal (oxy)hydroxides as the true active phase. Concurrently, their "leaching–re-adsorption" dynamic equilibrium mechanism not only accelerates the evolution of the active phase but also optimizes the electronic structure of active sites through re-adsorption, stabilizing key intermediates and achieving self-activation and self-regulation of catalytic performance. Secondly, acting as typical Brønsted bases, oxyanions can serve as "proton relays" to accelerate proton-coupled electron transfer processes. Leveraging their multi-step ionization characteristics, they construct a dynamic pH buffer layer at the electrode/electrolyte interface, mitigating the adverse effects of a local acidic microenvironment on catalyst stability. Furthermore, the introduction of oxyanions optimizes the adsorption behaviour of oxygen-containing intermediates, breaking the scaling relationship between *OOH and *OH inherent in the traditional AEM and even altering the rate-determining step of the reaction, thereby significantly reducing the overpotential. More importantly, oxyanions can activate the lattice oxygen mechanism by enhancing the covalency of metal–oxygen bonds, circumventing the thermodynamic limitations of the AEM to achieve higher intrinsic activity. Simultaneously, the induced oxygen vacancies and rapid OH^- adsorption capability

 This journal is © The Royal Society of Chemistry 2026

Table 1 Summary of the diverse mechanistic roles and corresponding catalytic effects of various oxyanions in OER electrocatalysts discussed in this review

Types of oxyanions	Mechanistic roles	Corresponding catalytic effects	Original context reference
PO_4^{3-}	Proton transfer	Acts as a ''proton bus'' to accelerate intermediate deprotonation	Section 3.2
	Reconstruction induction	Induces surface reconstruction to active Ni(Fe)OOH	Section 2.1
	Altering RDS	Changes the RDS to intermediate dehydrogenation	Section 4.2
	Interlayer expansion	Expands the LDH interlayer to expose more active sites	Section 6.1
SO_4^{2-}	Reconstruction induction	Accelerates precatalyst reconstruction to high-valence phases	Section 2.1
	LOM activation	Promotes oxygen vacancy generation to thermodynamically favor LOM	Section 5
	Intermediate adsorption	Breaks the OER scaling relationship *via* secondary hydrogen bonds with *OOH	Section 4.1
	Cl^- repulsion	Blocks Cl^- *via* electrostatic repulsion in seawater OER	Section 6.3
MoO_4^{2-}	Dynamic leaching–readsorption	Leaches to drive reconstruction, then readsorbs to tune electronic structure and suppress Cl^- corrosion	Section 2.3 and Section 6.3
	Altering RDS	Shifts the RDS from *OH to *O formation	Section 4.2
NO_3^-	Hydrophilicity enhancement	Adsorption significantly lowers the contact angle, facilitating bubble release and mass transfer	Section 4.3
	Dynamic leaching–readsorption	Readsorbs to stabilize *OOH intermediates	Section 2.3
	Inhibiting metal leaching	Forms a protective layer to suppress metal segregation and leaching	Section 6.2
CO_3^{2-}	Microenvironment regulation	Maintains a stable local alkaline microenvironment, mitigating acid-induced corrosion	Section 3.3
	Enhancing M–O covalency	Enhances Fe–O bond covalency, reducing the leaching tendency of active Fe atoms	Section 6.2
SeO_4^{2-}	Reconstruction induction	Leaching accelerates the transformation to active MOOH phases	Section 2.1
	LOM activation	Broadens Ni e_g orbitals to enhance M–O covalency, driving high valence species and oxygen vacancy generation	Section 5.1
VO_3^-	Dynamic leaching–readsorption	Promotes the formation of abundant oxygen vacancies during leaching	Section 2.3
	Vacancy engineering	Readsorbs to optimize OH^- adsorption and lower the RDS energy barrier	Section 2.3
WO_4^{2-}	Microenvironment regulation	Dynamically store and supply H^+	Section 3.3
$BO_3^{3-}/B(OH)_4^-$	Proton transfer	Acts as a strong base/proton acceptor to accelerate proton transfer rates	Section 3.1
	Interlayer expansion	Expands LDH interlayer distance to significantly increase the exposure of metal active sites	Section 6.1
Sq^{2-}	Microenvironment regulation	Captures OH^- *via* hydrogen bonds to delay the formation of a local acidic microenvironment, thereby enhancing catalyst stability	Section 3.3
Organic oxyanions (*e.g.*, $RCOO^-$, CH_3COO^-)	Proton transfer	Acts as a built-in base to capture protons and balance the PCET process	Section 3.1
	Interlayer expansion	Expands physical space between layers to facilitate electrolyte diffusion, gas release, and active site exposure	Section 6.1
CrO_4^{2-}	Cl^- repulsion	Blocks interfering Cl^- *via* electrostatic repulsion to suppress side reactions and anode corrosion in seawater OER	Section 6.3

contribute to establishing an ''activation–regeneration'' balance for lattice oxygen, suppressing metal dissolution and structural collapse. Additionally, oxyanions can expand the interlayer spacing of layered materials to expose more active sites, enhance hydrophilicity to optimize mass transfer, and inhibit chloride ion corrosion in seawater electrolysis through electrostatic repulsion, demonstrating excellent anti-interference ability. Overall, through synergistic regulatory mechanisms involving electrons, protons, the microenvironment, and reaction pathways, oxyanions hold immense promise for enhancing both the activity and stability of the OER. Table 1 systematically summarizes the diverse regulatory roles of the various oxyanions in the OER discussed in this review. Despite the significant progress achieved in oxyanion modulation as indicated by current research, the academic community still requires more systematic investigations to overcome the challenges currently facing the field.

Firstly, there is the issue concerning the existing forms of oxyanions. Upon introduction into OER catalysts, these oxyanions can exist in several forms, including surface adsorption, interlayer intercalation, lattice incorporation, and site anchoring. Surface adsorption can be further categorized into chemisorption, physisorption, and electrostatic adsorption of solvated ions. Interlayer intercalation involves anions residing within the interlayer spaces of the catalyst. Lattice incorporation refers to direct doping into the host lattice structure of the catalyst. Site anchoring describes immobilization within the catalyst structure through strong bonding interactions with specific elements, or direct coordination as ligands with the active metals. Notably, these existing forms do not exist in

isolation. Instead, they are subject to dynamic transformations and competitive relationships. For instance, anions intercalated within the host layers of some catalysts can readily leach out during the reaction and transform into a surface-adsorbed state, re-participating in the interfacial reaction. Furthermore, when oxyanions are added as additives to the electrolyte, they can either adsorb onto the surface or intercalate into the layers, with these two processes being competitive.[36] This elusive dynamic behaviour poses challenges for characterizing their existing forms, constructing theoretical calculation models, and elucidating structure–activity relationships. To address this, it is imperative to develop more *in situ* characterization techniques to obtain information on the bonding states and geometric structures of oxyanions. This also reminds us that future design of catalytic materials could shift from a static anchoring, forced confinement approach towards a concept emphasizing dynamic modulation and multi-component synergy, thereby achieving more efficient and stable catalytic processes.

Secondly, although the previous sections have systematically summarized the various pathways through which the introduction of oxyanions enhances OER performance, this regulatory strategy still faces several non-negligible limitations and challenges in practical applications. First, the interaction strength and surface coverage of oxyanions on the catalyst must be precisely controlled. If the binding of oxyanions is too strong or their surface coverage is excessively high, it will lead to the blockage of metal active sites and induce steric hindrance effects.[38,198–201] For example, computational results on the IrO_2 (110) surface model indicate that at a potential of 1.6 V (*vs.* RHE), the binding strengths of HPO_4^{2-} and HSO_4^- to the surface even exceed those of the OER intermediates, causing a severe site blocking effect. The results further confirm that $H_2PO_4^-$/HPO_4^{2-}, HSO_4^-/SO_4^{2-}, NO_3^-, Br^- and I^- all tend to bind strongly to the IrO_2 (110) surface, carrying the risk of poisoning the active Ir sites.[199] Second, complex dynamic competitive adsorption presents another severe challenge. This problem is particularly pronounced in catalytic systems where the regulating oxyanions primarily exist in an adsorbed state. The target oxyanions, the core reactants in the electrolyte, the oxygen containing intermediates generated during the reaction, and even impurity ions in the electrolytic system (such as Cl^- in seawater) undergo continuous dynamic competitive adsorption on the limited active sites of the catalyst.[199,202–204] If this competitive relationship cannot be effectively regulated, this will hinder the effective adsorption and mass transfer of reactants and key reaction intermediates, thereby disrupting the normal progression of the catalytic reaction pathway and reducing the intrinsic activity and reaction selectivity of the catalyst. Therefore, researchers should focus on constructing dynamic compensation and defence mechanisms within the catalytic system. By combining *in situ* characterization and dynamic simulation techniques, it is possible to achieve both thermodynamic and kinetic equilibrium at the catalytic interface under realistic reaction conditions. Furthermore, the long-term structural stability of electrocatalysts regulated by oxyanions remains a major challenge. Under OER anodic potentials and acidic/alkaline conditions, oxyanions, whether adsorbed on the surface or doped into the crystal lattice, may experience structural instability, thereby disrupting the material's unique coordination environment.[205,206] During long-term operation, the irreversible leaching of these regulatory oxyanions leads to a gradual decline in catalytic activity, making it difficult to meet the stringent durability requirements of industrial scale water splitting devices.[207] Consequently, finding the optimal balance between maximizing the promotional effects of oxyanions and suppressing their potential negative impacts is key to developing future commercial OER electrocatalysts.

Finally, there remains a lack of clarity regarding which specific oxyanions are suitable for which types of catalysts, posing difficulties for researchers in efficiently and precisely constructing catalyst systems with targeted anion modulation effects. With the progression of time and the evolution of research methodologies, it is anticipated that machine learning (ML) approaches can be leveraged. By utilizing extensive experimental and computational databases, it may become possible to establish qualitative, and even quantitative, structure–activity relationships between anions and catalytic performance. This could significantly shorten research cycles and enhance research efficiency.

Although the oxyanion modulation strategy still faces the aforementioned challenges, it has already demonstrated significant application potential in overcoming the traditional thermodynamic and kinetic bottlenecks of OER, as well as enhancing catalytic efficiency and stability. In the future, it is anticipated that by integrating more advanced characterization techniques, theoretical calculation methods, and performance prediction tools, the modulation mechanisms and structure–activity relationships of oxyanions can be further elucidated. This will enable the precise construction of OER catalysts possessing both excellent intrinsic activity and structural stability, thereby paving the way for their practical application in large-scale industrial water electrolysis.

Conflicts of interest

There are no conflicts to declare.

Data availability

No primary research results, software or code have been included and no new data were generated or analysed as part of this review.

Acknowledgements

This work was financially supported by the National Natural Science Foundation of China (No. 22209049) and the Natural Science Foundation of Guangdong Province (No. 2025A1515010003 and 2023A1515012804).

 This journal is © The Royal Society of Chemistry 2026

Notes and references

1 H. Li, Y. Lin, J. Duan, Q. Wen, Y. Liu and T. Zhai, *Chem. Soc. Rev.*, 2024, **53**, 10709–10740.
2 S. Sebbahi, A. Assila, A. Alaoui Belghiti, S. Laasri, S. Kaya, E. K. Hlil, S. Rachidi and A. Hajjaji, *Int. J. Hydrogen Energy*, 2024, **82**, 583–599.
3 J. Liang, X. Gao, B. Guo, Y. Ding, J. Yan, Z. Guo, E. C. M. Tse and J. Liu, *Angew. Chem., Int. Ed.*, 2021, **60**, 12770–12774.
4 Q.-N. Bian, B.-S. Guo, D.-X. Tan, D. Zhang, W.-Q. Kong, C.-B. Wang and Y.-Y. Feng, *ACS Appl. Mater. Interfaces*, 2024, **16**, 14742–14749.
5 K. Li, J. He, X. Guan, Y. Tong, Y. Ye, L. Chen and P. Chen, *Small*, 2023, **19**, 2302130.
6 Z. Xu, C.-L. Yeh, J.-L. Chen, J. T. Lin, K.-C. Ho and R. Y.-Y. Lin, *ACS Sustainable Chem. Eng.*, 2022, **10**, 11577–11586.
7 P. Chen, T. Zhou, S. Wang, N. Zhang, Y. Tong, H. Ju, W. Chu, C. Wu and Y. Xie, *Angew. Chem., Int. Ed.*, 2018, **57**, 15471–15475.
8 Y. Jiao, Y. Zheng, M. Jaroniec and S. Z. Qiao, *Chem. Soc. Rev.*, 2015, **44**, 2060–2086.
9 M. N. Khrizanforov, A. P. Samorodnova, I. A. Bezkishko, R. R. Gainullin, K. V. Kholin, A. T. Gubaidullin, R. P. Shekurov and V. A. Miluykov, *Mater. Rep.: Energy*, 2025, **5**, 100334.
10 X. Xu, C.-K. Peng, Y.-G. Lin and Z. Shao, *ChemElectroChem*, 2025, **12**, e202500326.
11 Z. Chen, L. Guo, L. Pan, T. Yan, Z. He, Y. Li, C. Shi, Z.-F. Huang, X. Zhang and J.-J. Zou, *Adv. Energy Mater.*, 2022, **12**, 2103670.
12 H.-F. Wang, C. Tang, B.-Q. Li and Q. Zhang, *Inorg. Chem. Front.*, 2018, **5**, 521–534.
13 W. Liao, H.-L. Su, S.-X. Mo, Y. Cao, H. Wang, H. Yu and H.-F. Wang, *Adv. Mater.*, 2026, e72791.
14 J. Duan, S. Chen, A. Vasileff and S. Z. Qiao, *ACS Nano*, 2016, **10**, 8738–8745.
15 B.-Q. Li, S.-Y. Zhang, C. Tang, X. Cui and Q. Zhang, *Small*, 2017, **13**, 1700610.
16 C.-X. Zhao, B.-Q. Li, M. Zhao, J.-N. Liu, L.-D. Zhao, X. Chen and Q. Zhang, *Energy Environ. Sci.*, 2020, **13**, 1711–1716.
17 C. Yang, Y. Zhu, F. Zhang, L. Yao, Y. Chen, T. Lu, Q. Li, J. Li, G. Wang, Q. Cheng and H. Yang, *Adv. Mater.*, 2025, **37**, 2507560.
18 S. Ding, Z. Li, G. Lin, Y. Ding, L. Wang and L. Sun, *Angew. Chem.*, 2025, **137**, e202517132.
19 J. Wang, S.-J. Kim, J. Liu, Y. Gao, S. Choi, J. Han, H. Shin, S. Jo, J. Kim, F. Ciucci, H. Kim, Q. Li, W. Yang, X. Long, S. Yang, S.-P. Cho, K. H. Chae, M. G. Kim, H. Kim and J. Lim, *Nat. Catal.*, 2021, **4**, 212–222.
20 H. F. Wang, C. Tang, B. Wang, B. Q. Li and Q. Zhang, *Adv. Mater.*, 2017, **29**, 1702327.
21 P.-W. Zhong, H.-X. Yang, W. Xu, Z. Yu, B. Li, Y. Jin, H. Wang, Y. Cao, H.-F. Wang, Y. Yang and H. Yu, *React. Chem. Eng.*, 2026, DOI: 10.1039/D5RE00397K.
22 M. Gu, L. Jiang, H. Wang, Q. Chen, Y. Hao, L. Li, F. Hu, X. Zhang, Y. Wu, G. Wang and S. Peng, *J. Am. Chem. Soc.*, 2025, **147**, 19675–19686.
23 J. Zheng, Z.-J. Chen, W. Lu, J. Wu, T. Zhang, L. Zhang, S. Bao, S. Ming, B. Feng, F. Meng, H. Jin, Y. Sun, J. Peng and C. Wu, *J. Am. Chem. Soc.*, 2026, **148**, 217–227.
24 W. Zhao, J. Gu, H.-S. Chang, B. Deng, Y. Long, Z. Zhang, R. Ma, X. He, J. Liu, K. Huang, Y. Li, Y. Shao, H. Wu and J. Lu, *Adv. Funct. Mater.*, 2026, e28941.
25 Y. Tang, C. Wu, Q. Zhang, H. Zhong, A. Zou, J. Li, Y. Ma, H. An, Z. Yu, S. Xi, J. Xue, X. Wang and J. Wu, *Angew. Chem.*, 2023, **135**, e202309107.
26 R. Fan, S. Lu, F. Wang, Y. Zhang, M. Hojamberdiev, Y. Chai, B. Dong and B. Zhang, *Nat. Commun.*, 2025, **16**, 3407.
27 Y. Liu, X. Jiao, X. Jiang, C. Xing, X. Qi, X. Wang and A. Cabot, *ACS Nano*, 2026, **20**, 6732–6741.
28 J.-H. Park, H. J. Kwon, D. Y. Lee and S.-J. Suh, *Small*, 2024, **20**, 2400046.
29 X. Du, J. Zhang, M. Zhang, H. Wei, X. Lin, W. Guo, P. Zhang and Z. Luo, *Green Chem.*, 2025, **27**, 7380–7388.
30 A. K. Satheesan, V. Parey, A. Karmakar, R. Madhu, S. Nagappan, S. Singha Roy, P. Mazumder, R. Thangamuthu, S. Chakraborty and S. Kundu, *Small*, 2025, **21**, e08560.
31 W. Wang, Q. Wen, D. Huang, Y. Lin, N. Zhao, L. Tang, M. Li, Y. Liu and R. He, *Angew. Chem., Int. Ed.*, 2025, **64**, e202415132.
32 M. Guo, P. Li, A. Wang, J. Wang, J. Chen, F. Lei, P. Hao, X. Sun, J. Xie and B. Tang, *Chem. Commun.*, 2023, **59**, 5098–5101.
33 Y. Yu, W. Zhou, J. Yuan, X. Zhou, X. Zhang, X. Li, X. Xia, L. Zhang, Y. Chen, X. Meng, X. Wang, F. Sun, J. Gao and G. Zhao, *Nat. Commun.*, 2026, **17**, 3014.
34 Y. Che, J. Shang, Y. Zhang, S. Bo, J. Zhang, X. Qin, X. Liu, H. Sun, W. Zhou, Y. Jiang, X. Chen, S. He, D. Ma, F. Pan and Q. Liu, *Adv. Funct. Mater.*, 2025, **35**, 2507544.
35 W. Bao, J. Liu, T. Ai, J. Han, J. Hou, W. Li, X. Wei, X. Zou, Z. Deng and J. Zhang, *Adv. Funct. Mater.*, 2024, **34**, 2408364.
36 J. N. Hausmann and P. W. Menezes, *Angew. Chem., Int. Ed.*, 2022, **61**, e202207279.
37 H.-M. Zhang, *Nano Energy*, 2024, **129**, 110089.
38 Z. Liu, G. Ma, X. Zhu, Y. Shen, X. Guo, Y. Ding, J. Liu, D. Khalafallah, X. Huang, B. Guo and S. Li, *ACS Energy Lett.*, 2026, **11**, 1514–1537.
39 Z. He, M. Ajmal, M. Zhang, X. Liu, Z.-F. Huang, C. Shi, R. Gao, L. Pan, X. Zhang and J.-J. Zou, *Adv. Sci.*, 2023, **10**, 2304071.
40 T. Nishimoto, T. Shinagawa, T. Naito and K. Takanabe, *ChemSusChem*, 2021, **14**, 1554–1564.
41 H. Komiya, T. Shinagawa and K. Takanabe, *ChemSusChem*, 2022, **15**, e202201088.
42 H. Komiya, K. Obata, M. Wada, T. Nishimoto and K. Takanabe, *ACS Sustainable Chem. Eng.*, 2023, **11**, 12614–12622.
43 M. Kadowaki, T. Moronaga, A. Nakamura, Y. Murase, T. Hashimoto, H. Katayama, K. Takanabe and Y. Tsutsumi, *J. Phys. Chem. C*, 2025, **129**, 15939–15948.
44 B. M. Hunter, W. Hieringer, J. R. Winkler, H. B. Gray and A. M. Müller, *Energy Environ. Sci.*, 2016, **9**, 1734–1743.
45 Y. Xu, Y. Hao, G. Zhang, Z. Lu, S. Han, Y. Li and X. Sun, *RSC Adv.*, 2015, **5**, 55131–55135.
46 L. Dang, H. Liang, J. Zhuo, B. K. Lamb, H. Sheng, Y. Yang and S. Jin, *Chem. Mater.*, 2018, **30**, 4321–4330.
47 J. A. Carrasco, R. Sanchis-Gual, A. S.-D. Silva, G. Abellán and E. Coronado, *Chem. Mater.*, 2019, **31**, 6798–6807.
48 X. Xue, F. Yu, J.-G. Li, G. Bai, H. Yuan, J. Hou, B. Peng, L. Chen, M.-F. Yuen, G. Wang, F. Wang and C. Wang, *Int. J. Hydrogen Energy*, 2020, **45**, 1802–1809.
49 F. Kong, H. Zhang, C. Wang, G. Zhang, J. Zhang, X. Gao, T. Zhang, S. Chu, L. Song and S. Tao, *J. Energy Chem.*, 2026, **114**, 946–954.
50 X.-Q. Ren, M.-X. Chen, X. Cao, Y.-L. Dai, W.-X. Yu, Z. Liu, X.-X. Wen, G.-X. Ma, B.-R. Guo, S.-X. Tan, J. Liu, P. Xu, J.-J. Gao and S.-W. Li, *Rare Met.*, 2025, **44**, 5498–5511.
51 X. Li, J. Wang, H. Xue, L. Zhao, J. Lu, H. Zhang, M. Yan, F. Deng and C. Hu, *Adv. Funct. Mater.*, 2025, **35**, 2503360.
52 W. Zheng and L. Y. S. Lee, *ACS Energy Lett.*, 2021, **6**, 2838–2843.
53 H. Zhong, Q. Zhang, J. Yu, X. Zhang, C. Wu, Y. Ma, H. An, H. Wang, J. Zhang, X. Wang and J. Xue, *Adv. Energy Mater.*, 2023, **13**, 2301391.
54 Z. Chen, R. Zheng, M. Grąś, W. Wei, G. Lota, H. Chen and B.-J. Ni, *Appl. Catal., B*, 2021, **288**, 120037.
55 X. Liu, F. Xia, R. Guo, M. Huang, J. Meng, J. Wu and L. Mai, *Adv. Funct. Mater.*, 2021, **31**, 2101792.
56 X. Liu, J. Meng, K. Ni, R. Guo, F. Xia, J. Xie, X. Li, B. Wen, P. Wu, M. Li, J. Wu, X. Wu, L. Mai and D. Zhao, *Cell Rep. Phys. Sci.*, 2020, **1**, 100241.
57 Y. Cao, R. Abazari, Q. Li and J. Qian, *Chem. Soc. Rev.*, 2026, **55**, 5227–5268.
58 N. Heidary, M. Morency, D. Chartrand, K. H. Ly, R. Iftimie and N. Kornienko, *J. Am. Chem. Soc.*, 2020, **142**, 12382–12393.
59 H. Jia, N. Yao, Z. Liao, L. Wu, J. Zhu, Y. Lao and W. Luo, *Angew. Chem., Int. Ed.*, 2024, **63**, e202408005.
60 Y. Lin, L. Yu, L. Tang, F. Song, R. Schlögl and S. Heumann, *ACS Catal.*, 2022, **12**, 5345–5355.
61 H. Wang, H. Liu, Y. Cao, N. Li, Y. Fu, X. Zhou, Q. Li and J. Qian, *J. Colloid Interface Sci.*, 2026, **702**, 138865.
62 H. Liao, T. Luo, P. Tan, K. Chen, L. Lu, Y. Liu, M. Liu and J. Pan, *Adv. Funct. Mater.*, 2021, **31**, 2102772.
63 R. Liang, B. Zhang, Y. Du, X. Han, S. Li and P. Xu, *ACS Catal.*, 2023, **13**, 8821–8829.
64 Y. Wang, Y. Zhu, S. Zhao, S. She, F. Zhang, Y. Chen, T. Williams, T. Gengenbach, L. Zu, H. Mao, W. Zhou, Z. Shao, H. Wang, J. Tang, D. Zhao and C. Selomulya, *Matter*, 2020, **3**, 2124–2137.
65 S. Li, Z. Li, R. Ma, C. Gao, L. Liu, L. Hu, J. Zhu, T. Sun, Y. Tang, D. Liu and J. Wang, *Angew. Chem., Int. Ed.*, 2021, **60**, 3773–3780.
66 Y. Shi, W. Du, W. Zhou, C. Wang, S. Lu, S. Lu and B. Zhang, *Angew. Chem., Int. Ed.*, 2020, **59**, 22470–22474.

67 H. Ma, Y. Ding, J. Li, W. Peng and L. Mai, *Nano Res.*, 2024, **17**, 7975–7983.
68 B. Dasgupta, S. Ghosh, C. Walter, M. S. Budde, G. J. Marquardt, H.-H. Chen, M. G. M. Breithaupt, T. Yilmaz, C. Garmatter, T. Ahamad, I. Zebger, M. Driess and P. W. Menezes, *J. Mater. Chem. A*, 2024, **12**, 30522–30533.
69 X. Liu, J. Meng, J. Zhu, M. Huang, B. Wen, R. Guo and L. Mai, *Adv. Mater.*, 2021, **33**, 2007344.
70 Z. Chen, H. Yang, Z. Kang, M. Driess and P. W. Menezes, *Adv. Mater.*, 2022, **34**, 2108432.
71 Y. Zhang, W. Zhang, X. Zhang, J. Li and G. Liu, *J. Energy Chem.*, 2025, **101**, 676–684.
72 H. Lei, L. Ma, Q. Wan, S. Tan, B. Yang, Z. Wang, W. Mai and H. J. Fan, *Adv. Energy Mater.*, 2022, **12**, 2202522.
73 X. Wang, X. Han, R. Du, Z. Liang, Y. Zuo, P. Guardia, J. Li, J. Llorca, J. Arbiol, R. Zheng and A. Cabot, *Appl. Catal., B*, 2023, **320**, 121988.
74 N. C. S. Selvam, L. Du, B. Y. Xia, P. J. Yoo and B. You, *Adv. Funct. Mater.*, 2021, **31**, 2008190.
75 X. Liu, J. Meng, J. Zhu, M. Huang, B. Wen, R. Guo and L. Mai, *Adv. Mater.*, 2021, **33**, e2007344.
76 Y. Dong, S. Komarneni, F. Zhang, N. Wang, M. Terrones, W. Hu and W. Huang, *Appl. Catal., B*, 2020, **263**, 118343.
77 Y. Dong, S. Komarneni, N. Wang, W. Hu and W. Huang, *J. Mater. Chem. A*, 2019, **7**, 6995–7005.
78 T. Kahlstorf, J. Niklas Hausmann, I. Mondal, K. Laun, I. Zebger, T. Sontheimer and P. W. Menezes, *Green Chem.*, 2023, **25**, 8679–8686.
79 X. Cui, Y. Ding, T. Tang, L. Wang, F. Zhang, P. Li, L. Sun and B. Zhang, *ACS Appl. Mater. Interfaces*, 2025, **17**, 29659–29668.
80 X. Kang, F. Yang, Z. Zhang, H. Liu, S. Ge, S. Hu, S. Li, Y. Luo, Q. Yu, Z. Liu, Q. Wang, W. Ren, C. Sun, H.-M. Cheng and B. Liu, *Nat. Commun.*, 2023, **14**, 3607.
81 H. Liao, X. Zhang, S. Niu, P. Tan, K. Chen, Y. Liu, G. Wang, M. Liu and J. Pan, *Appl. Catal., B: Environ. Energy*, 2022, **307**, 121150.
82 Y. Ma, M.-X. Lin, P.-J. Su, Z.-Y. Gao, X. Li, Y.-H. Wang, L.-M. Zhao, Y.-M. Chai and B. Dong, *Chem. Eng. J.*, 2024, **500**, 157263.
83 J. Liu, X. He, Y. Wang, Z. Sun, Y. Liu, B. Liu, H. Li, F. Guo and X. Li, *J. Alloys Compd.*, 2022, **927**, 167060.
84 J. Zhou, L. Liu, H. Ren, L. Li, W. Song, N. Li, X. Shi, C. Kou, Y. Sun, M. Han, H. Wang, J. Han, K. Liu, C. D. Momo, Y. Liu, D. Feng, W. Zhu, S. Chen, H. Jiang, Y. Liu and H. Liang, *Inorg. Chem. Front.*, 2024, **11**, 498–507.
85 Y. Jin, X. Qu, Z. Zhou, R. Liu, M. Zhang, L. Song, W. Ma and M. Zhang, *Small*, 2025, **21**, 2408171.
86 G. Fu, W. Li, J. Y. Zhang, M. Li, C. Li, N. Li, Q. He, S. Xi, D. Qi, J. L. MacManus-Driscoll, J. Cheng and K. H. Zhang, *Small*, 2021, **17**, e2006930.
87 A. Grimaud, O. Diaz-Morales, B. Han, W. T. Hong, Y.-L. Lee, L. Giordano, K. A. Stoerzinger, M. T. M. Koper and Y. Shao-Horn, *Nat. Chem.*, 2017, **9**, 457–465.
88 M. Liu, N. Li, S. Cao, X. Wang, X. Lu, L. Kong, Y. Xu and X.-H. Bu, *Adv. Mater.*, 2022, **34**, 2107421.
89 Q. Wang, Y. Gong, X. Zi, L. Gan, E. Pensa, Y. Liu, Y. Xiao, H. Li, K. Liu, J. Fu, J. Liu, A. Stefancu, C. Cai, S. Chen, S. Zhang, Y.-R. Lu, T.-S. Chan, C. Ma, X. Cao, E. Cortés and M. Liu, *Angew. Chem., Int. Ed.*, 2024, **63**, e202405438.
90 Z. Pu, R. Cheng, J. Zhao, Z. Hu, C. Li, W. Li, P. Wang, I. S. Amiinu, Z. Wang, W. Min, D. Chen and S. Mu, *iScience*, 2020, **23**, 101793.
91 C.-X. Zhao, H.-F. Wang, B.-Q. Li and Q. Zhang, *Acc. Mater. Res.*, 2021, **2**, 1082–1092.
92 Y. Meng, G. Ni, X. Jin, J. Peng and Q. Y. Yan, *Mater. Today Nano*, 2020, **12**, 100095.
93 X. Yin, X. Dai, F. Nie, Z. Ren, Z. Yang, Y. Gan, B. Wu, Y. Cao and X. Zhang, *Nanoscale*, 2021, **13**, 14156–14165.
94 M. Liu, N. Li, X. Wang, J. Zhao, D.-C. Zhong, W. Li and X.-H. Bu, *Angew. Chem., Int. Ed.*, 2023, **62**, e202300507.
95 K. Feng, D. Zhang, F. Liu, H. Li, J. Xu, Y. Xia, Y. Li, H. Lin, S. Wang, M. Shao, Z. Kang and J. Zhong, *Adv. Energy Mater.*, 2020, **10**, 2000184.
96 W. Liu, D. Zheng, T. Deng, Q. Chen, C. Zhu, C. Pei, H. Li, F. Wu, W. Shi, S.-W. Yang, Y. Zhu and X. Cao, *Angew. Chem., Int. Ed.*, 2021, **60**, 10614–10619.
97 S. Ding, B. Zheng, X. Wang, Y. Zhou, Z. Pan, Y. Chen, G. Liu and L. Lang, *Langmuir*, 2024, **40**, 10384–10392.
98 M. W. Kanan and D. G. Nocera, *Science*, 2008, **321**, 1072–1075.
99 D. K. Bediako, Y. Surendranath and D. G. Nocera, *J. Am. Chem. Soc.*, 2013, **135**, 3662–3674.
100 Y. Surendranath, M. Dincă and D. G. Nocera, *J. Am. Chem. Soc.*, 2009, **131**, 2615–2620.
101 T. Liu, Y. Chen, Y. Hao, J. Wu, R. Wang, L. Gu, X. Yang, Q. Yang, C. Lian, H. Liu and M. Gong, *Chem*, 2022, **8**, 2700–2714.
102 Y. Hao, Y. Kang, S. Wang, Z. Chen, C. Lei, X. Cao, L. Chen, Y. Li, Z. Liu and M. Gong, *Angew. Chem., Int. Ed.*, 2023, **62**, e202303200.
103 X. Wang, M. Cheng, Z. Chen, Z. Wang, C. Li, S. Sun and S. Hu, *Appl. Surf. Sci.*, 2023, **622**, 156896.
104 P. Jiang, Q. Liu, Y. Liang, J. Tian, A. M. Asiri and X. Sun, *Angew. Chem., Int. Ed.*, 2014, **53**, 12855–12859.
105 T. Irebo, S. Y. Reece, M. Sjödin, D. G. Nocera and L. Hammarström, *J. Am. Chem. Soc.*, 2007, **129**, 15462–15464.
106 D. K. Zhong, M. Cornuz, K. Sivula, M. Grätzel and D. R. Gamelin, *Energy Environ. Sci.*, 2011, **4**, 1759–1764.
107 Y. Zhang, J. Wang, M. Tan, Z. Wang, W. Cen, L. Li, L. Zou, H. Kang, M. Li, X. Wang, N. Wang, S. Chen, Y. Zhu and J. Deng, *ACS Sustainable Chem. Eng.*, 2025, **13**, 13837–13853.
108 S. Mukhopadhyay, O. Basu, A. Kar and S. K. Das, *Inorg. Chem.*, 2020, **59**, 472–483.
109 Z. Guan, L. Zhang, Y. Xie, D. Wu, B. Yuan, L. Wu, G. Shen, G. Tan and F. Guo, *J. Colloid Interface Sci.*, 2026, **702**, 139037.
110 C. Hong, J. Lu, Y. Bian, W. Huang, H. Wang, M. Shi, X. Zheng and Y. Deng, *Small*, 2025, **21**, 2504396.
111 J. Qi, Q. Chen, Y. Gao, Y. Zhao, S. Gao, E. Shangguan and M. Chen, *ChemSusChem*, 2025, **18**, e202401932.
112 S. Geiger, O. Kasian, M. Ledendecker, E. Pizzutilo, A. M. Mingers, W. T. Fu, O. Diaz-Morales, Z. Li, T. Oellers, L. Fruchter, A. Ludwig, K. J. J. Mayrhofer, M. T. M. Koper and S. Cherevko, *Nat. Catal.*, 2018, **1**, 508–515.
113 W. Liu, X. Ding, J. Cheng, J. Jing, T. Li, X. Huang, P. Xie, X. Lin, H. Ding, Y. Kuang, D. Zhou and X. Sun, *Angew. Chem., Int. Ed.*, 2024, **63**, e202406082.
114 F.-Y. Chen, Z.-Y. Wu, Z. Adler and H. Wang, *Joule*, 2021, **5**, 1704–1731.
115 D. Y. Chung, P. P. Lopes, P. F. B. D. Martins, H. He, T. Kawaguchi, P. Zapol, H. You, D. Tripkovic, D. Strmcnik, Y. Zhu, S. Seifert, S. Lee, V. R. Stamenkovic and N. M. Markovic, *Nat. Energy*, 2020, **5**, 222–230.
116 Z. Li, Y. Zhou, M. Xie, H. Cheng, T. Wang, J. Chen, Y. Lu, Z. Tian, Y. Lai and G. Yu, *Angew. Chem., Int. Ed.*, 2023, **62**, e202217815.
117 X. Liu, X. Zhao, S. Cao, M. Xu, Y. Wang, W. Xue and J. Li, *Appl. Catal., B*, 2023, **331**, 122715.
118 W. Li, Y. Ding, Y. Zhao, Z. Li, G. Lin, L. Wang and L. Sun, *Angew. Chem., Int. Ed.*, 2025, **64**, e202505924.
119 M. Yu, J. Li, F. Liu, J. Liu, W. Xu, H. Hu, X. Chen, W. Wang and F. Cheng, *J. Energy Chem.*, 2022, **72**, 361–369.
120 I. C. Karagiannis and P. G. Soldatos, *Desalination*, 2008, **223**, 448–456.
121 W. Tong, M. Forster, F. Dionigi, S. Dresp, R. Sadeghi Erami, P. Strasser, A. J. Cowan and P. Farràs, *Nat. Energy*, 2020, **5**, 367–377.
122 J. E. Bennett, *Int. J. Hydrogen Energy*, 1980, **5**, 401–408.
123 D. W. Kirk and A. E. Ledas, *Int. J. Hydrogen Energy*, 1982, **7**, 925–932.
124 D. Bao, L. Huang, Y. Gao, K. Davey, Y. Zheng and S.-Z. Qiao, *J. Am. Chem. Soc.*, 2024, **146**, 34711–34719.
125 X. Lu, J. Pan, E. Lovell, T. H. Tan, Y. H. Ng and R. Amal, *Energy Environ. Sci.*, 2018, **11**, 1898–1910.
126 W. Zhu, Z. Wei, Y. Ma, M. Ren, X. Fu, M. Li, C. Zhang, J. Wang and S. Guo, *Angew. Chem., Int. Ed.*, 2024, **63**, e202319798.
127 M. T. M. Koper, *J. Electroanal. Chem.*, 2011, **660**, 254–260.
128 I. C. Man, H.-Y. Su, F. Calle-Vallejo, H. A. Hansen, J. I. Martínez, N. G. Inoglu, J. Kitchin, T. F. Jaramillo, J. K. Nørskov and J. Rossmeisl, *ChemCatChem*, 2011, **3**, 1159–1165.
129 N. Yao, P. Li, Z. Zhou, Y. Zhao, G. Cheng, S. Chen and W. Luo, *Adv. Energy Mater.*, 2019, **9**, 1902449.
130 C. Lin, J.-L. Li, X. Li, S. Yang, W. Luo, Y. Zhang, S.-H. Kim, D.-H. Kim, S. S. Shinde, Y.-F. Li, Z.-P. Liu, Z. Jiang and J.-H. Lee, *Nat. Catal.*, 2021, **4**, 1012–1023.
131 Y. Chen, Q. Li, Y. Lin, J. Liu, J. Pan, J. Hu and X. Xu, *Nat. Commun.*, 2024, **15**, 7278.
132 Z. Duan, Z. Cui, Z. Gao, W. Xu, Y. Liang, H. Jiang, Z. Li, F. Wang and S. Zhu, *ACS Catal.*, 2025, **15**, 16882–16892.

This journal is © The Royal Society of Chemistry 2026

133 Y. Xue, J. Fang, X. Wang, Z. Xu, Y. Zhang, Q. Lv, M. Liu, W. Zhu and Z. Zhuang, *Adv. Funct. Mater.*, 2021, **31**, 2101405.
134 R. Zhang, L. Wang, L. Pan, Z. Chen, W. Jia, X. Zhang and J.-J. Zou, *Appl. Catal., B*, 2020, **277**, 119237.
135 Q. Ye, J. Liu, L. Lin, M. Sun, Y. Wang and Y. Cheng, *Nanoscale*, 2022, **14**, 6648–6655.
136 M. Hyder, A. D. O'Donnell, A. M. Chippindale, I. M. German, J. L. Harries, O. Shebanova, I. W. Hamley and W. Hayes, *Mater. Today Chem.*, 2022, **26**, 101008.
137 X. Wu, X. Song, H. Tan, Y. Kang, Z. Zhao, S. Jin and X. Chang, *Mater. Today Chem.*, 2022, **26**, 101008.
138 F. Luo, P. Yu, J. Xiang, J. Jiang and S. Chen, *J. Energy Chem.*, 2024, **94**, 508–516.
139 S. Zhou, H. He, J. Li, Z. Ye, Z. Liu, J. Shi, Y. Hu and W. Cai, *Adv. Funct. Mater.*, 2024, **34**, 2313770.
140 L. Shao, X. Han, L. Shi, T. Wang, Y. Zhang, Z. Jiang, Z. Yin, X. Zheng, J. Li, X. Han and Y. Deng, *Adv. Energy Mater.*, 2024, **14**, 2303261.
141 C. F. Dickens, C. Kirk and J. K. Nørskov, *J. Phys. Chem. C*, 2019, **123**, 18960–18977.
142 Y. Xue, J. Zhao, L. Huang, Y.-R. Lu, A. Malek, G. Gao, Z. Zhuang, D. Wang, C. T. Yavuz and X. Lu, *Nat. Commun.*, 2023, **14**, 8093.
143 Y. Liu, S. Zhang, C. Jiao, H. Chen, G. Wang, W. Wu, Z. Zhuo and J. Mao, *Adv. Sci.*, 2023, **10**, 2206107.
144 W. He, S. Wu, Z. Zhang, P. Duan and Q. Yang, *Int. J. Hydrogen Energy*, 2024, **51**, 44–54.
145 R. Gan, Q. Zhao, Y. Ran, Q. Ma, G. Cheng, L. Fang, Y. Zhang and D. Wang, *J. Colloid Interface Sci.*, 2025, **687**, 724–732.
146 X. H. Zhang, H. L. Zhang, Z. X. Chen, X. D. Chen, J. Y. Wang, S. X. Wei, S. Y. Liu, Z. J. Wang, F. N. Dai, M. H. Wang and X. Q. Lu, *Adv. Funct. Mater.*, 2025, **35**, 2418940.
147 X. Wang, H. Zhong, S. Xi, W. S. V. Lee and J. Xue, *Adv. Mater.*, 2022, **34**, e2107956.
148 N. Han, W. Zhang, W. Guo, H. Pan, B. Jiang, L. Xing, H. Tian, G. Wang, X. Zhang and J. Fransaer, *Nano-Micro Lett.*, 2023, **15**, 185.
149 X. Zhang, H. Zhang, Z. Chen, X. Chen, J. Wang, S. Wei, S. Liu, Z. Wang, F. Dai, M. Wang and X. Lu, *Adv. Funct. Mater.*, 2025, **35**, 2418940.
150 L. Ke, Y. Wang, X. Jiang, X. Wang, K. Zhao, Y. Wan and N. Yan, *Nat. Commun.*, 2025, **16**, 11241.
151 H. Zhong, Q. Zhang, W. Cui, H. Wen, G. Sun, J. Yu, C. Wu, Z.-G. Yu, T. Xiong, S. Xi and J. Xue, *Adv. Energy Mater.*, 2026, **13**, 2301391.
152 S. Liu, M. Sun, L. Dai, S. Wang, Z. Yu, N. Li, F. Chen, Y. Wei, Y. Shen, C. Zhao and M. Wang, *Nat. Commun.*, 2026, **17**, 2135.
153 Y. Pan, X. Xu, Y. Zhong, L. Ge, Y. Chen, J.-P. M. Veder, D. Guan, R. O'Hayre, M. Li, G. Wang, H. Wang, W. Zhou and Z. Shao, *Nat. Commun.*, 2020, **11**, 2002.
154 X. Xu, Y. Pan, Y. Zhong, C. Shi, D. Guan, L. Ge, Z. Hu, Y.-Y. Chin, H.-J. Lin, C.-T. Chen, H. Wang, S. P. Jiang and Z. Shao, *Adv. Sci.*, 2022, **9**, 2200530.
155 P. Zhang, J. Wang, T. Yang, R. Wang, R. Shen, Z. Peng, Y. Liu, X. Wu, J. Jiang and B. Li, *Chin. J. Catal.*, 2025, **72**, 48–83.
156 Z. H. Xue, J. Mahmood, Y. X. Shang, G. X. Li, S. J. Kim, Y. Han and C. T. Yavuz, *J. Am. Chem. Soc.*, 2025, **147**, 17839–17848.
157 Y. Liu, K. Ba, P. Li, Y. Lin and T. Xie, *Langmuir*, 2025, **41**, 9256–9263.
158 J. Wang, H. Zhao, H. Zhang, R. Huang, S. Zheng, H. Li, J. Cai, Y. Li, X. Liu and X. Deng, *Renewable Energy*, 2025, **242**, 122385.
159 X. Tao, L. Hou, X. Wang, J. Jin, H. Li and F. Gao, *Nat. Commun.*, 2025, **16**, 8788.
160 C. Li, B. Ye, B. Ouyang, T. Zhang, T. Tang, Z. Qiu, S. Li, Y. Li, R. Chen, W. Wen, M. Song, B. Mei, X. Xia and Y. Zhang, *Adv. Mater.*, 2025, **37**, 2501381.
161 J. Han, H. Wang, Y. Wang, H. Zhang, J. Li, Y. Xia, J. Zhou, Z. Wang, M. Luo, Y. Wang, N. Wang, E. Cortés, Z. Wang, A. Vomiero, Z.-F. Huang, H. Ren, X. Yuan, S. Chen, D. Feng, X. Sun, Y. Liu and H. Liang, *Angew. Chem., Int. Ed.*, 2024, **63**, e202405839.
162 J. T. Mefford, X. Rong, A. M. Abakumov, W. G. Hardin, S. Dai, A. M. Kolpak, K. P. Johnston and K. J. Stevenson, *Nat. Commun.*, 2016, **7**, 11053.
163 Z.-F. Huang, J. Song, Y. Du, S. Xi, S. Dou, J. M. V. Nsanzimana, C. Wang, Z. J. Xu and X. Wang, *Nat. Energy*, 2019, **4**, 329–338.
164 S. Sen and T. K. Mandal, *ChemCatChem*, 2025, **17**, e00535.
165 X. Zhong, H.-Y. Wang, C. Zhang, W. Wang, C. T. Nelson, X. He, Q. Sun, B. G. Gibson, M. Neupane, B. Deng, M. Liu and Y. Yang, *Adv. Funct. Mater.*, 2025, **35**, e18240.
166 Y. Qiu, R. Gao, W. Yang, L. Huang, Q. Mao, J. Yang, L. Sun, Z. Hu and X. Liu, *Chem. Mater.*, 2020, **32**, 1864–1875.
167 R. L. D. A. Loyo, S. I. Nikitenko, A. C. Scheinost and M. Simonoff, *Environ. Sci. Technol.*, 2008, **42**, 2451–2456.
168 M. Kang, F. Chen, S. Wu, Y. Yang, C. Bruggeman and L. Charlet, *Environ. Sci. Technol.*, 2011, **45**, 2704–2710.
169 M. Cai, Q. Liu, Z. Xue, Y. Li, Y. Fan, A. Huang, M.-R. Li, M. Croft, T. A. Tyson, Z. Ke and G. Li, *J. Mater. Chem. A*, 2020, **8**, 190–195.
170 T. Zhang, Y. Liu, L. Tong, J. Yu, S. Lin, Y. Li and H. J. Fan, *ACS Nano*, 2023, **17**, 6770–6780.
171 N.-T. Suen, S.-F. Hung, Q. Quan, N. Zhang, Y.-J. Xu and H. M. Chen, *Chem. Soc. Rev.*, 2017, **46**, 337–365.
172 Y. Zhai, X. Ren, Y. Sun, D. Li, B. Wang and S. Liu, *Appl. Catal., B*, 2023, **323**, 122091.
173 S. Li, S. Zhao, S.-F. Hung, L. Deng, L. Wang, F. Shi, A. Dong, Y. Zhang, T.-Y. Chen, F. Hu, L. Li, S. Ramakrishna, Y. Wu and S. Peng, *J. Am. Chem. Soc.*, 2025, **147**, 33770–33779.
174 F. Wu, F. Tian, M. Li, S. Geng, L. Qiu, L. He, L. Li, Z. Chen, Y. Yu, W. Yang and Y. Hou, *Angew. Chem., Int. Ed.*, 2025, **64**, e202413250.
175 X. Wang, J. Li, Q. Xue, X. Han, C. Xing, Z. Liang, P. Guardia, Y. Zuo, R. Du, L. Balcells, J. Arbiol, J. Llorca, X. Qi and A. Cabot, *ACS Nano*, 2023, **17**, 825–836.
176 X. He, M. Liu, F. Liu, X. Liu, H. Liao, P. Tan and J. Pan, *Adv. Funct. Mater.*, 2025, **35**, e05936.
177 C. Wei, S. Sun, D. Mandler, X. Wang, S. Z. Qiao and Z. J. Xu, *Chem. Soc. Rev.*, 2019, **48**, 2518–2534.
178 R.-Q. Yao, Y.-T. Zhou, H. Shi, Q.-H. Zhang, L. Gu, Z. Wen, X.-Y. Lang and Q. Jiang, *ACS Energy Lett.*, 2019, **4**, 1379–1386.
179 J. N. Hausmann, S. Mebs, K. Laun, I. Zebger, H. Dau, P. W. Menezes and M. Driess, *Energy Environ. Sci.*, 2020, **13**, 3607–3619.
180 L. Li, Y. Dai, Q. Xu, B. Zhang, F. Zhang, Y. You, D. Ma, S.-S. Li and Y.-X. Zhang, *J. Alloys Compd.*, 2021, **882**, 160752.
181 L. Su, H. Du, C. Tang, K. Nan, J. Wu and C. Ming Li, *J. Colloid Interface Sci.*, 2018, **528**, 36–44.
182 X. He, J. Cai, Q. Chen, J. Liu, Q. Zhong, J. Liu, Z. Sun, D. Qu, Y. Lu and X. Li, *New J. Chem.*, 2023, **47**, 19484–19493.
183 X. Wang, R. Ma, S. Li, M. Xu, L. Liu, Y. Feng, T. Thomas, M. Yang and J. Wang, *Adv. Energy Mater.*, 2023, **13**, 2300765.
184 Y. Zhang, X. Zhang, Y. Gao, W. Li, Q. Zhao, J. Li and G. Liu, *J. Colloid Interface Sci.*, 2026, **701**, 138678.
185 H. Over, *Chem. Rev.*, 2012, **112**, 3356–3426.
186 S. Hao, M. Liu, J. Pan, X. Liu, X. Tan, N. Xu, Y. He, L. Lei and X. Zhang, *Nat. Commun.*, 2020, **11**, 5368.
187 H. Liao, G. Ni, P. Tan, K. Liu, X. Liu, H. Liu, K. Chen, X. Zheng, M. Liu and J. Pan, *Adv. Mater.*, 2023, **35**, 2300347.
188 J. Chang, G. Wang, Z. Yang, B. Li, Q. Wang, R. Kuliiev, N. Orlovskaya, M. Gu, Y. Du, G. Wang and Y. Yang, *Adv. Mater.*, 2021, **33**, 2101425.
189 T. Ma, W. Xu, B. Li, X. Chen, J. Zhao, S. Wan, K. Jiang, S. Zhang, Z. Wang, Z. Tian, Z. Lu and L. Chen, *Angew. Chem., Int. Ed.*, 2021, **60**, 22740–22744.
190 S. Jung Kim, H. Choi, J. Ho Ryu, K. Min Kim, S. Mhin, A. Kumar Nayak, J. Bang, M. Je, G. Ali, K. Yoon Chung, K.-H. Na, W.-Y. Choi, S. Yeo, J. Uk Jang and H. Han, *J. Energy Chem.*, 2023, **81**, 82–92.
191 L. Tan, J. Yu, C. Wang, H. Wang, X. Liu, H. Gao, L. Xin, D. Liu, W. Hou and T. Zhan, *Adv. Funct. Mater.*, 2022, **32**, 2200951.
192 L. Cheng, D. Cai, Y. He, S. Geng, Y. Wang and S. Song, *ACS Sustainable Chem. Eng.*, 2024, **12**, 16365–16377.
193 L. Guo, J. Chi, T. Cui, J. Zhu, Y. Xia, H. Guo, J. Lai and L. Wang, *Adv. Energy Mater.*, 2024, **14**, 2400975.
194 P. Tian, W. Zong, J. Xiong, W. Liu, J. Liu, Y. Dai, J. Zhu, S. Huang, S. Song, K. Chu, G. He and N. Han, *Adv. Funct. Mater.*, 2025, **35**, 2504862.
195 H.-M. Zhang, L. Zuo, Y. Gao, J. Guo, C. Zhu, J. Xu and J. Sun, *J. Mater. Sci. Technol.*, 2024, **173**, 1–10.
196 Z. Li, Y. Yao, S. Sun, J. Liang, S. Hong, H. Zhang, C. Yang, X. Zhang, Z. Cai, J. Li, Y. Ren, Y. Luo, D. Zheng, X. He, Q. Liu, Y. Wang, F. Gong, X. Sun and B. Tang, *Angew. Chem., Int. Ed.*, 2024, **63**, e202316522.

197 L. Ye, Y. Ding, X. Niu, X. Xu, K. Fan, Y. Wen, L. Zong, X. Li, X. Du and T. Zhan, *J. Colloid Interface Sci.*, 2024, **665**, 240–251.
198 I. T. E. Fonseca, M. I. Lopes and M. T. C. Portela, *J. Electroanal. Chem.*, 1996, **415**, 89–96.
199 S. A. K. Navodye and G. T. K. K. Gunasooriya, *J. Phys. Chem. C*, 2024, **128**, 6041–6052.
200 A. Ganassin, V. Colic, J. Tymoczko, A. S. Bandarenka and W. Schuhmann, *Phys. Chem. Chem. Phys.*, 2015, **17**, 8349–8355.
201 J. A. Arminio-Ravelo, A. W. Jensen, K. D. Jensen, J. Quinson and M. Escudero-Escribano, *Chem. Phys. Chem.*, 2019, **20**, 2956–2963.
202 Q. Wu, Q. Gao, C. Zhang, J. Wang, J. Li, F. Yang, S. Sun, M. S. Hamdy, A. Farouk and X. Sun, *Green Chem.*, 2026, **28**, 7552–7585.
203 J. Mo, J. Shi, W. Cai and L. Feng, *J. Mater. Chem. A*, 2026, **14**, 10487–10504.
204 D.-Y. Kuo, J. K. Kawasaki, J. N. Nelson, J. Kloppenburg, G. Hautier, K. M. Shen, D. G. Schlom and J. Suntivich, *J. Am. Chem. Soc.*, 2017, **139**, 3473–3479.
205 D. Guan, G. Ryu, Z. Hu, J. Zhou, C.-L. Dong, Y.-C. Huang, K. Zhang, Y. Zhong, A. C. Komarek, M. Zhu, X. Wu, C.-W. Pao, C.-K. Chang, H.-J. Lin, C.-T. Chen, W. Zhou and Z. Shao, *Nat. Commun.*, 2020, **11**, 3376.
206 Z. Li, Y. Zhu, M. Zhang, A. Zhang and L. Wang, *Chem. Commun.*, 2025, **61**, 18507–18541.
207 W. Park and D. Y. Chung, *ACS Mater. Au*, 2025, **5**, 1–10.

This journal is © The Royal Society of Chemistry 2026